Linear Melt Rheology and Small-Angle X-ray Scattering of AB Diblocks vs A 2 B 2 Four Arm Star Block Copolymers

8 AUTHORS, INCLUDING:

David Martin Buzza
University of Hull

34 PUBLICATIONS **564** CITATIONS

SEE PROFILE

R. N. Young
The University of Sheffield

34 PUBLICATIONS **1,159** CITATIONS

SEE PROFILE

Ian W Hamley
University of Reading

398 PUBLICATIONS **11,771** CITATIONS

SEE PROFILE

Linear Melt Rheology and Small-Angle X-ray Scattering of AB Diblocks vs A₂B₂ Four Arm Star Block Copolymers

D. M. A. Buzza,*,†,‡ A. H. Fzea,§,∥ J. B. Allgaier,∥ R. N. Young,∥ R. J. Hawkins,‡ I. W. Hamley,⊥ T. C. B. McLeish,‡ and T. P. Lodge#

Department of Physics and Astronomy & Polymer IRC, University of Leeds, Leeds LS2 9JT, U.K.; Department of Chemistry, University of Sheffield, Sheffield S3 7HF, U.K.; School of Chemistry, University of Leeds, Leeds LS2 9JT, U.K.; and Department of Chemical Engineering and Materials Science, University of Minnesota, Minneapolis, Minnesota 55455

ABSTRACT: The frequency dependent viscoelastic properties and lamellar spacing of three symmetric styrene−isoprene (PS−PI) diblock copolymers are compared to those of their hetero-four-arm star counterparts. The PS and PI arm molecular weights of the three linear and three star samples are 10, 20, and 60 kg/mol, respectively. All six samples were unoriented and had lamellar morphology for temperatures less than T_{ODT}, the order−disorder temperature for each molecular weight. The lamellar spacing D at the same temperature was found to scale with overall molecular weight N according to $D \sim N^{\delta}$, with $\delta \approx 0.7$ for both linear and stars. However, the star chains were consistently 5−10% more strongly stretched compared to their linear counterparts. For the 10K arm materials, the critical frequency for the onset of mesophase relaxations (ω_c) for the stars was found to be about 20 times smaller compared to the linears. This difference correlated very well with quantitative estimates of the inverse layer hopping time of the chains, suggesting that mesophase relaxations for the 10K arm materials may be controlled by layer hopping of chains. For the 10K and 20K arm materials, relaxation of the PS chain deformations are dominant for $\omega \gg \omega_{term}^{PS}$, whereas nonclassical terminal scaling of G', $G'' \sim \omega^{1/2}$ was observed for $\omega \ll \omega_{term}^{PS}$ and $T < T_{ODT}$ due to mesophase relaxations (ω_{term}^{PS} is the PS block terminal relaxation frequency). In addition, the linear rheology of the linear and star analogues coincide for $\omega \gg \omega_{term}^{PS}$, but an additional shoulder emerges in the star materials for $\omega \approx \omega_{term}^{PS}$. By fitting to a simple model incorporating free chain Rouse dynamics and mesophase relaxations, we were able to obtain excellent quantitative fits to the 20K materials across the whole frequency range and conclude that the observed shoulder in the star materials was due to differences in the linear and star mesophase relaxations. The fitted ω_c and G_{M0} (the mesophase modulus) values are in good agreement with Kawasaki−Onuki theory indicating that the mesophase relaxations of the 20K arm materials may be controlled by collective hydrodynamic layer fluctuations rather than layer hopping of chains. For the 60K arm materials, qualitatively different behavior compared to the lower molecular weight samples was observed: PI rate controlled relaxation with G', $G'' \sim \omega^{1/2}$ was observed for $\omega \gg \omega_{term}^{PS}$. We identify this relaxation as a PI controlled *mesophase* relaxation. Theoretical estimates of ω_c for this mechanism using Kawasaki−Onuki theory yield $\omega_c \gg \omega_{term}^{PS}$ in support of our suggestion.

I. Introduction

Block copolymers are macromolecules where sequences, or blocks, of chemically distinct repeat units are covalently bonded together within the same molecule. One of the most striking features of these macromolecules is that, in the melt phase, the distinct chemical units microphase separate at low enough temperatures to form ordered microdomains whose length scale is of the order of the size of a molecule. This transition is called the order−disorder transition (ODT) and the temperature at which it occurs is known as the order−disorder transition temperature (T_{ODT}). For $T > T_{ODT}$, the system is in the disordered state and its rheology is similar to that of homopolymer melts. However, qualitatively different behavior is observed for

$T < T_{ODT}$ for frequencies below the terminal frequency for molecular relaxations. Because of formation of microdomains, nonclassical terminal behavior, sensitive to the symmetry of the microdomain morphology, is observed.[1] Until relatively recently, most rheological studies on block copolymers have tended to focus on block copolymers with simple linear architecture, notably on diblocks and triblocks.[1−10] However, advances in synthetic chemistry, especially in the area of anionic polymerization, have allowed block copolymers with more complex molecular architectures, specifically those with branched architecture, to be synthesized. This has opened up a whole new dimension in block copolymer research, namely the influence of molecular architecture and topology on solution and melt properties of block copolymers. For some examples of studies on the dynamical properties of block copolymers with complex molecular architecture, see refs 11−13.

For well entangled homopolymers, the presence of long chain branching has a dramatic effect on dynamical and rheological behaviors. The theory is particularly well-developed for the rheology of homopolymers with the simplest branched architecture, namely that of

† E-mail: dmabuzza@leeds.ac.uk.
‡ Department of Physics and Astronomy & Polymer IRC, University of Leeds.
§ Present address: Department of Chemistry, University of Dundee, Dundee DD1 4HN, U.K.
∥ University of Sheffield.
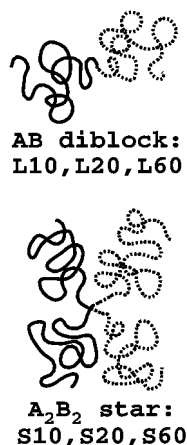⊥ School of Chemistry, University of Leeds.
University of Minnesota.

AB diblock:
L10,L20,L60

A₂B₂ star:
S10,S20,S60

Figure 1. AB diblock vs A_2B_2 hetero-arm star block copolymer.

stars, which contain a single branch point.[14,15] To explore the effect of branched architecture on block copolymer rheology, we report here results for symmetric polystyrene (PS)−polyisoprene (PI) AB diblock copolymers compared to their hetero-four-arm star analogues A_2B_2 (see Figure 1). Block copolymers with A_nB_n architecture have been successfully synthesized by various co-workers using anionic polymerization.[16−19] A_2B_2 can be thought of as being made up of two AB diblocks joined together at the block junction to form a star polymer; as such, it represents the simplest branched block copolymer. The resultant A_2B_2 is thermodynamically similar to the constituent AB diblocks, but we expect the presence of the branch point to lead to different dynamical behavior. To study the effect of PS and PI entanglement on block copolymer rheology, a total of three diblock copolymers with different PS and PI block lengths (labeled L10, L20, L60) were synthesized together with their hetero-arm star counterparts, labeled S10, S20, and S60, respectively. The PS and PI arm molecular weights are about 10 kg/mol for L10 and S10, 20 kg/mol for L20 and S20 and 60 kg/mol for L60 and S60. The block lengths were chosen so that for L10 and S10, both PI and PS blocks are nominally unentangled, for L20 and S20 only the PI block is entangled, and for L60 and S60, both PS and PI blocks are entangled. (The critical weight for entanglements for PI and PS homopolymers is respectively $M_c^{PS} \approx 30$ kg/mol, $M_c^{PI} \approx 10$ kg/mol.[20])

A first attempt at studying AB vs A_2B_2 rheology was made by Johnson et al.[11] Unfortunately, for the nonsymmetric compositions used, comparison of the linear and star data was complicated by the fact that linear and star analogues did not necessarily have the same morphology. The use of symmetric block copolymers allows us to overcome this problem since both stars and linears in this case are theoretically predicted and experimentally confirmed to have lamellar morphology (see subsection III.A). Mean-field theory predicts symmetric AB and A_2B_2 to be thermodynamically identical.[21,22] In fact, a previous study has revealed that the linear and star analogues have significantly different T_{ODT}.[22] This is believed to be due to compositional fluctuations and additional non-Gaussian chain stretching in A_2B_2 induced by the star branch point, both effects not being accounted for in the mean-field theory. Including both these effects within the framework of a simple model calculation reproduced differences in T_{ODT} between AB and A_2B_2 comparable to experimental

values.[22] Notwithstanding this technical complication, the linear and star samples are similar enough thermodynamically as to allow for meaningful comparison of their rheology.

Most previous studies on block copolymer dynamics have focused on the mesophase relaxation regime. For more strongly incompatible block copolymers, e.g., PS−PI, this has necessitated the use of low molecular weight samples in order to have experimentally accessible values of T_{ODT}. This has however meant that the molecular relaxation spectra is only accessible over a narrow frequency range using conventional rheometers because of the very short terminal molecular relaxation times. This shortcoming is overcome in our study by the use of higher molecular weight block copolymers (i.e., L20, S20, L60, and S60). Although this means that T_{ODT} is no longer accessible for all these samples, the use of higher weights allows us to probe more fully the rheology for frequencies above the molecular terminal relaxation frequencies. Interestingly, we find qualitatively different behavior for these higher molecular weight samples *both* below and above the molecular terminal relaxation frequencies. For L20 and S20 we find, in contrast to the 10K arm materials, that the mesophase relaxations appear to be controlled by collective hydrodynamic layer fluctuations rather than chain hopping events (see subsection III C). For L60 and S60, we find novel and hitherto unexpected partial relaxation of mesophase stress at frequencies higher than the PS terminal molecular relaxation frequency (see subsection III.D).

A brief outline of the paper is as follows. Section II is the Experimental Section, where details of the synthesis and characterization of the block copolymers as well as of the small-angle X-ray scattering (SAXS) and rheology measurements are given. Section III constitutes the bulk of the paper, where the SAXS and rheology results are presented and discussed for all six copolymer samples. Finally in section IV, we give a summary of our main findings as well as suggestions for future work.

II. Experimental Section

A. Synthesis and Characterization. The general procedure of the synthesis of both the linear and star samples has been outlined elsewhere.[22] After synthesis, the molecular weight and dispersity of the samples were determined using SEC (size-exclusion chromotography) and osmometry. The composition of all six samples was also determined by ^{1}H NMR spectroscopy using a Bruker AC250 instrument. The glass transition temperature (T_g) of the PS phase was determined using DSC with a heating rate of 10 °C/min. The molecular weight, dispersity and composition data are collected in Table 1 while the T_g(PS) data are collected in Table 2.

The order−disorder transition temperature (T_{ODT}) of L10 and S10 has been measured previously using rheology and SAXS[22] and was found to be $T_{ODT} \approx 158$ °C for L10 and $T_{ODT} \approx 200$ °C for S10. The rheology measurements are repeated in subsection III.B, and good agreement is found with the previous measurement. The T_{ODT} of the higher molecular weight samples can be estimated theoretically from Fredrickson-Helfand fluctuation theory.[22,23] This gives $(\chi N)_{ODT}$ for symmetric AB diblocks and A_2B_2 stars to be, respectively

$$(\chi N)_{ODT} = 10.5 + 41\bar{N}^{-1/3} \tag{1}$$

$$(\chi N)_{ODT} = 10.5 + 34\bar{N}^{-1/3} \tag{2}$$

where χ is the Flory interaction parameter between A and B monomers, N is the total number of monomers in an AB

Table 1. Molecular Weight and Dispersity Data for Styrene−Isoprene Block Copolymers]

	isoprene arm (SEC)		styrene arm (SEC)		copolymer		
sample	M_n, kg mol^{-1}	M_w/M_n	M_n, kg mol^{-1}	M_w/M_n	(osmom) M_n, kg mol^{-1}	(SEC) M_w/M_n	(NMR) wt % styrene
L10	10.8[a]		10.3	1.02	21.1[b]	1.01	48
L20	20.5[a]		20.9	1.01	41.4	1.01	51
L60	63.5[a]		61.5	1.01	125	1.01	50
S10	9.7	1.02	10.3	1.02	40.0[c]	1.01	49
S20	19.9	1.01	21.0	1.02	81.6	1.01	48
S60	56.8	1.01	61.6	1.01	239	1.02	50

[a] Calculated from M_n(copolymer) − M_n(styrene arm). M_n(copolymer) corrected for composition. [b] Determined from SEC. [c] M_w determined by static light scattering.

Table 2. Thermodynamic and Thermorheological Properties of the Styrene−Isoprene Block Copolymers[a]

sample	T_g(PS)/°C	T_{ODT}/°C	q^*(140 °C)/Å^{-1}	$c_1(T_0 = 140$ °C)	$c_2(T_0 = 140$ °C)
L10	75	159[b]	0.0360	7.06	139
S10	82	198[b]	0.0328	5.96	105
L20	90	263[c]	0.0221	5.18	81.0
S20	95	269[c]	0.0205	5.59	73.6
L60	100	370[c]	0.0099	1.26 (high ω)	48.9 (high ω)
				7.04[d] (low ω)	89.8[d] (low ω)
S60	102.5	371[c]	0.0094	2.11[e] (high ω)	237[e] (high ω)
				7.04[d] (low ω)	89.8[d] (low ω)

[a] Note that the top and bottom sets of c_1 and c_2 coefficients for L60 and S60 correspond to the values used to superpose the high and low ω data, respectively. [b] Determined from rheology. [c] Theoretical estimate using method described in subsection II.A. [d] c_1, c_2 for pure PS (ref 20). [e] c_1, c_2 for pure PI (ref 20).

diblock, and $\bar{N} = b^6/v^2 N$ with $b = 1/2 (b_A^2 + b_B^2)$ being the mean monomer length and $v = (v_A v_B)^{1/2}$ the mean monomer volume. Using the PS and PI parameter values given in Appendix A and the temperature dependent χ parameter given by[24]

$$\chi(T) = \frac{66}{T} - 0.0937 \tag{3}$$

we obtain T_{ODT} values for the higher molecular weight samples given in Table 2. The predicted T_{ODT}s are much higher than the sample degradation temperature ($\sim$ 200 °C)[11] and therefore could not be accessed experimentally.

B. Small-Angle X-ray Scattering. SAXS experiments were conducted at the Synchrotron Radiation Source, Daresbury Laboratory, Daresbury, U.K., on beamline 8.2. This beamline is configured with an X-ray wavelength λ = 1.5 Å. Details of the storage ring, radiation, camera geometry, and data collection electronics have been given elsewhere.[25] The sample in powder form was placed in a TA Instruments DSC pan fitted with 25 μm mica windows. Solvent casting was avoided to ensure that the sample was in an equilibrium state. The loaded pans were placed in the cell of a Linkam DSC of single-pan design. The cell comprised a silver furnace around a heat-flux plate with a 3 × 0.5 mm slot, the sample being held in contact with the plate by a low-thermal-mass spring. A more complete description of the DSC and the sample pans can be found elsewhere.[26] Scattered photons were collected on a multiwire quadrant positional sensitive detector located 2 m from the sample. A scattering pattern from an oriented specimen of wet collagen (rat-tail tendon) was used for calibration of the q scale range of the detector, ($q = 4\pi \sin \theta/\lambda$, where the scattering angle is defined as 2θ). The experimental data were corrected for background scattering (from the camera and empty shear cell), sample absorption, and the positional alinearity of the detector.

C. Rheology. Rheological measurements were performed using a Rheometrics RDAII rheometer. For L20, S20, L60, and S60, a 25 mm diameter parallel plate geometry was used. For L10 and S10, a 35 mm cup and plate geometry was used instead. This is because for the high strain amplitudes that were required to obtain measurable signals near the ODT, it was found that sample was expelled from the gap when a parallel plate geometry was used (presumably due to a flow instability). We have checked that for lower strains and temperatures, measurements performed with parallel plate

geometry and cup and plate geometry give essentially the same results. The larger plate diameter of the cup and plate geometry had the further advantage of producing a larger torque for a given strain, thus increasing the sensitivity of our measurements.

Samples for rheological measurements were prepared as follows. For L20, S20, L60, and S60, approximately 1 g of bulk polymer powder was pressed into a disk at room temperature, and the disk was then transferred into a vacuum oven and annealed at 120 °C for 24 h. After cooling to room temperature, the disk was placed in the rheometer oven and heated to 120 °C for L20 and S20 and 140 °C for L60 and S60 under nitrogen gas atmosphere for 1 h to remove any air bubbles. The disk was then squeezed between the plates to a gap of approximately 1 mm and a diameter of 25 mm. After cooling to room temperature, the oven door was opened and any excess material around the plates was removed by a sharp razor blade. The oven was closed again and the temperature was increased to 100 °C; this was maintained for 30 min with enough normal force applied on the plates for the polymer to conform to the plate diameter. For L10 and S10, approximately 1 g of bulk polymer powder was pressed into a disk at room temperature; the disk was then transferred into a vacuum oven and annealed at 80 °C for 48 h to remove any residual solvent. After cooling to room temperature, the disk was placed in the bottom cup plate of the rheometer and heated to 140 °C under nitrogen atmosphere for about 10 min to melt the sample into the shape of the cup geometry and to remove any bubbles formed in the drying process. The sample was then squeezed between the plates to a gap of approximately 1 mm.

The sample preparation procedure outlined above inevitably produces some lamellar alignment, especially during compression of the samples. However, given that the major part of the compression is carried out at room temperature, which is well below the T_g of the styrene phase, we expect the degree of alignment due to sample preparation to be minimal. This is confirmed by the fact that in subsequent dynamic frequency sweeps, we observe nonclassical terminal behavior for all our samples characteristic of lamellar phases with no long-range order in lamellar orientation.

To determine T_{ODT} for L10 and S10, dynamic temperature sweeps with temperatures decreasing or increasing at a rate of 5 °C were performed. A strain amplitude of 5% at a frequency of 1 rad/s was applied to the sample during cooling or heating. According to well-documented procedures[3,4] the
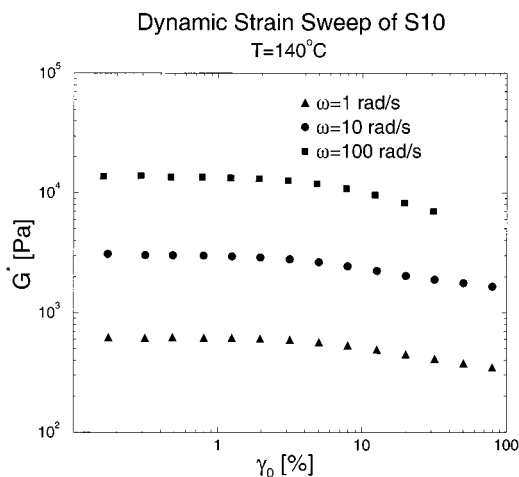
Figure 2. Dynamic strain sweep of S10 at three different frequencies. ($G^* = (G'^2 + G''^2)^{1/2}$.

order−disorder transition (ODT) can be identified by a sharp drop in G' on heating or a sharp rise in G' on cooling. To remove the residual effect of sample preparation history, each sample was subjected to the temperature sweep cycle twice and the result from the second sweep cycle was used to determine T_{ODT}.

Dynamic strain sweeps were performed to determine the extent of linear viscoelastic regime for all the samples. A typical plot is shown in Figure 2 for the case of S10. The strain sweeps show that the linear viscoelastic regime extends to approximately 2% for all the samples. Strain amplitudes of 2% were therefore used for all dynamic frequency sweep measurements where possible. However for L10 and S10, we found it necessary to use higher strain amplitudes (5−60%) as T_{ODT} was approached to compensate for the drop in modulus. For each polymer, dynamic frequency sweeps were carried out over a frequency range of 0.1−100 rad/s and a temperature range between 100 and 210 °C (at higher temperatures, a frequency range of 1−100 rad/s was used to minimize sample exposure to high temperatures). The lowest temperature used for each sample was 20−30 °C above the T_g of PS, to ensure that we have melt conditions. The highest temperature used did not exceed 210 °C because of problems with sample degradation above this temperature.[11] SEC traces of L10 and S10 were taken after the rheology tests to check for sample degradation as these samples were subjected to high temperatures. No measurable degradation was found for L10, and less than 1% degradation was found for S10.

III. Results and Discussion

A. Small-angle X-ray Scattering. In Figure 3, we plot the small-angle X-ray scattering powder diffraction pattern for all six samples measured at $T = 140$ °C while in Figure 4, the first-order reflection peak q^* is plotted as a function of the total polymerization number of the linear analogue N. The q^* values for all six samples are collected in Table 2. From indexing the reflection peaks in the SAXS patterns, the 20K and 60K arm materials (i.e., L20, S20, L60, S60) were confirmed to have lamellar morphology. The 10K arm materials (i.e., L10, S10) are only weakly segregated, and consequently only one order of reflection was observed. However, they are also expected to have lamellar morphology on the basis of composition. In addition, we have performed shear orientation experiments on these samples, and the resultant SAXS patterns from cut-up samples in three orthogonal planes are consistent with the samples having lamellar morphology with the lamellae oriented parallel to the shear plates. From Figure 3, we see that
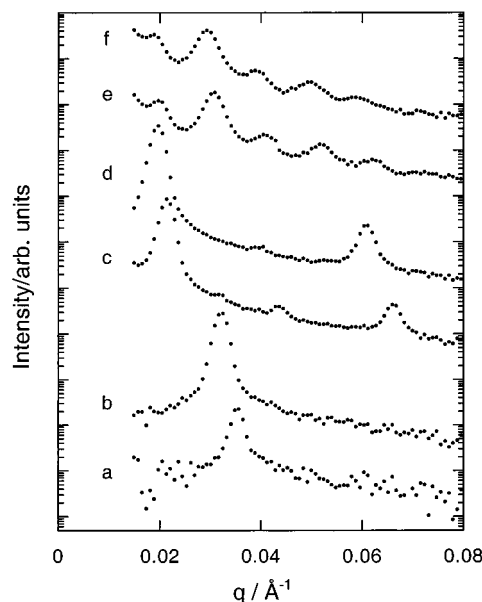

Figure 3. Small-angle X-ray scattering powder patterns for L10, S10, L20, S20, L60, and S60 (a−f respectively) obtained at 140 °C. Note that the first-order reflection peak q^* for L60 and S60 (e and f) is below the measured q range; however its position can be deduced from the position of higher order reflections. Note also the increasing number of higher order reflections that become visible with increasing molecular weight, indicating a stronger degree of phase segregation in the higher molecular weight systems.
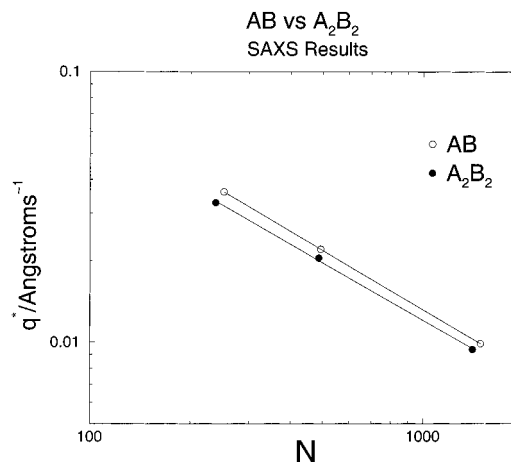

Figure 4. A log−log plot of the first-order reflection peak (q^*) as a function of the total polymerization number of one A block and one B block (N) for AB diblocks (unfilled) and A_2B_2 stars (filled). The solid lines are the best fit straight lines through the linear and star data, indicating power law scaling of $q^* \sim N^{-\delta}$, with $\delta = 0.73 \pm 0.04$ and 0.70 ± 0.04 for linears and stars, respectively.

the star polymers are consistently 5−10% more strongly stretched compared to their linear counterparts over all molecular weights, indicating stronger phase segregation in the stars. However both linear and stars show approximately the same scaling of q^* with respect to N, i.e., $q^* \sim N^{-\delta}$, with $\delta = 0.73 \pm 0.04$ for AB diblocks and $\delta = 0.70 \pm 0.04$ for A_2B_2 stars (see Figure 4). Here N is the total polymerization number of one A block and one B block calculated using the formula given in Appendix A, and the uncertainty in δ reflects a 5% uncertainty in molar masses and 1% uncertainty in q^* values.
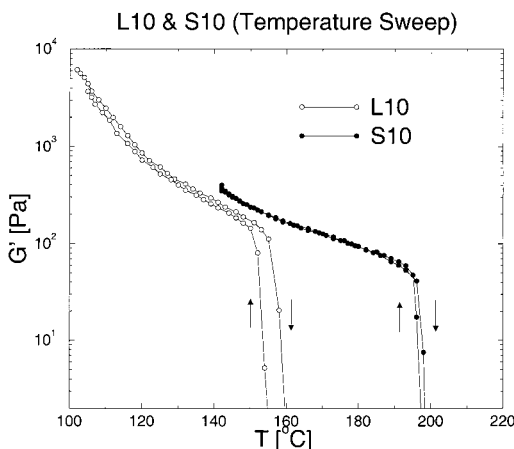
Figure 5. Dynamic storage modulus of L10 (unfilled) and S10 (filled) for increasing and decreasing temperature sweeps. The order–disorder transition in both samples is indicated by the sharp drop/rise in the storage modulus.

The values for the scaling exponent δ that we have found are in good agreement with self-consistent field theory (SCFT) calculations by Matsen and co-workers in the intermediate segregation regime, where $\delta \approx 0.7$ was found for both AB diblocks[27,28] and A_2B_2 stars[28] (for $\chi N \sim 30-100$). Our value for the AB diblock scaling exponent is also in good agreement with the value $\delta = 0.69 \pm 0.03$ found by Mai et al. for symmetric poly-(oxyethylene)–poly(oxybutylene) diblock copolymer melts.[27] SCFT calculations by Matsen et al. in the χN range covered by our experiments also found lamellar spacings for A_2B_2 stars to be 5–8% higher than the homologous AB diblocks,[28] again in good agreement with our measurements. Interestingly, Hadziioannou and Skoulios report a scaling exponent of $\delta = 0.79 \pm 0.02$ for styrene–isoprene diblock copolymers in the intermediate segregation regime,[29] which is higher than our value, but consistent with the value of $\delta = 0.80 \pm 0.04$ reported by Almdal et al. for poly(ethylene–propylene)–poly(ethylethylene) diblock copolymers.[30] One explanation for the difference between our results and that of Hadziioannou et al. and Almdal et al. might be that while all our samples are within the intermediate segregation regime relatively far from ODT, both Hadziioannou et al. and Almdal et al. include samples which are either weakly ordered or weakly disordered in their determination of δ. For these samples which are near the ODT, it is well-known that composition fluctuations can induce a strong degree of chain stretching. The inclusion of these data points in Hadziioannou et al. and Almdal et al. may therefore drive the overall scaling exponent to slightly higher values than the values that we have determined for δ.

B. Rheology of L10 and S10. Figure 5 shows the elastic modulus, G', for L10 and S10 for increasing and decreasing temperature sweeps. From the sharp drop (rise) in G', the T_{ODT} for L10 is determined to be between 155 and 159 °C and the T_{ODT} for S10 to be between 197 and 198 °C (the hysteresis in both sets of measurements is due to superheating/supercooling). This is in good agreement with our previous rheological and SAXS measurement of the T_{ODT} which yielded $T_{ODT} \approx 158$ °C for L10 and $T_{ODT} \approx 200$ °C for S10.[22] The significant difference in T_{ODT} between L10 and S10 is contrary to mean-field theory predictions. However as shown in ref 22, the experimental difference can be reproduced if one includes the effects of compositional fluctuations and
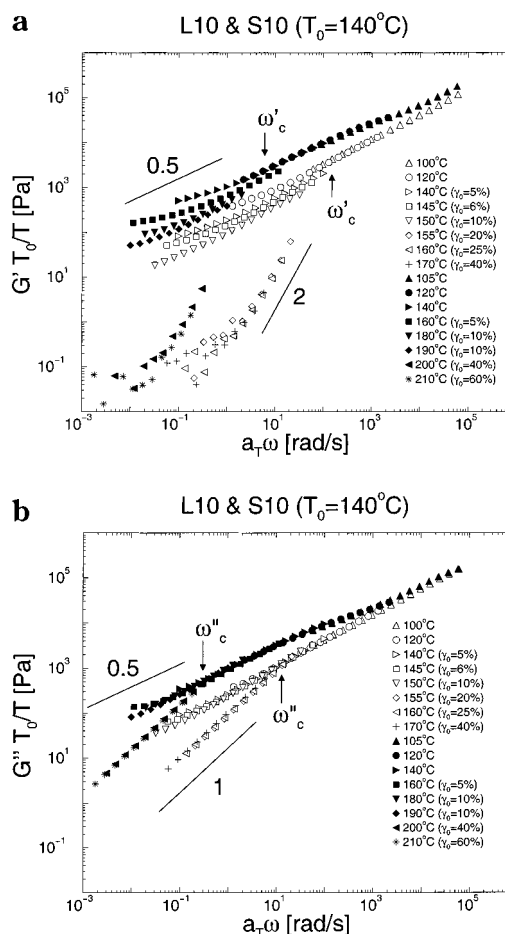

Figure 6. (a) Dynamic storage modulus and (b) dynamic loss modulus of L10 (unfilled) and S10 (filled) shifted to a reference temperature of $T_0 = 140$ °C. The critical frequency for the onset of mesophase relaxation (ω'_c for G', ω''_c for G'') for both L10 and S10 are indicated.

additional non-Gaussian chain stretching in A_2B_2 induced by the star branch point in the theoretical calculation.

Figure 6a shows G' (storage modulus) and Figure 6b shows G'' (loss modulus) as a function of frequency ω for L10 (open symbols) and S10 (filled symbols) for a range of temperatures, going from below to just above T_{ODT}. A strain amplitude of 2% was used at lower temperatures, however, as T_{ODT} was approached, it was found to be necessary to use higher strain amplitudes to compensate for the drop in modulus. The strains used at higher temperatures are indicated in Figure 6, parts a and b. A vertical shift of T_0/T was applied to account for the temperature dependence of the plateau modulus, where a reference temperature of $T_0 = 140$ °C was used. The data have also been shifted horizontally to superpose G'' data at high frequency. For both L10 and S10, the shift factors that produced superposition of the G'' data at high frequency also superposed the high frequency G' data, although for the highest temperatures in L10 and S10, the frequency at which the lower (disordered) G' branch merges with the upper (ordered) branch is above the frequency range of the rheometer. The horizontal shift factors a_T for L10 and S10 were found to fit the WLF form well[20]

$$\log a_T = \frac{-c_1(T-T_0)}{c_2 + T - T_0}$$

Shift Factors & WLF Curves
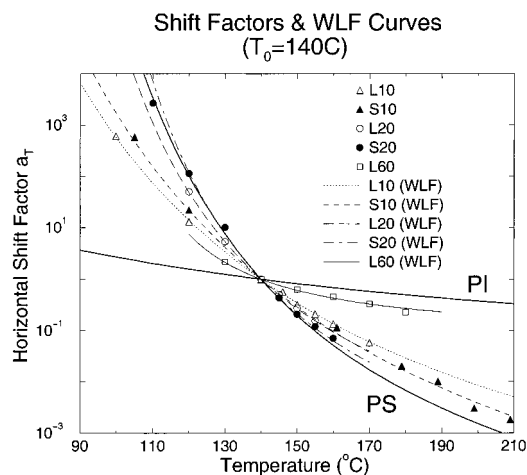### (T_0=140C)

Figure 7. Linear−log plot of horizontal shift factors a_T as a function of temperature and best fit WLF curves for L10, S10, L20, S20, and L60. The shift factors for L60 are those used to superpose the high-frequency part of the data. The WLF curves for pure PI and PS are also plotted for reference.

The horizontal shift factors a_T and the best fit WLF curves for L10 and S10 are shown in Figure 7 while the WLF parameters c_1 and c_2 are listed in Table 2.

Our results are in good agreement with previous rheological measurements on unoriented symmetric PS−PI diblocks with similar molecular weights.[7−9] For $T > T_{ODT}$, both G' and G'' clearly exhibit classical terminal scaling, i.e., $G' \sim \omega^2$, $G'' \sim \omega$ for both L10 and S10. For $T < T_{ODT}$, both classical scaling and time−temperature superposition fail for frequencies below a critical frequency, presumably due to the formation of microdomains. The resultant terminal regime scales roughly as G', $G'' \sim \omega^{1/2}$ and is intermediate between that of a newtonian liquid and a solid ($G' \sim \omega^0$); this agrees well with previous experimental measurements on unoriented lamellar phases.[2−5,7−9] Defining the critical frequency, $a_T\omega_c$ (or more specifically, $a_T\omega_c'$ for G' and $a_T\omega_c''$ for G'), as the point where the disordered branch of the rheology intersects the main branch, for $\omega < \omega_c$, the main contribution to the modulus arises from microdomain deformations, while for $\omega > \omega_c$, the modulus is dominated by single chain relaxations of PS and PI chains. For both L10, S10, we observe G', $G'' \sim \omega^{1/2}$ scaling at the highest frequencies; this is reasonable given that both the PI and PS blocks are unentangled so that we would expect Rouse scaling in this regime. The critical frequencies for L10 are approximately $a_T\omega_c' \approx 150$ rad/s, $a_T\omega_c'' \approx 13$ rad/s while for S10, $a_T\omega_c' \approx 6$ rad/s, $a_T\omega_c'' \approx 0.3$ rad/s; these are indicated in Figure 6, parts a and b. In agreement with other co-workers, we find that $a_T\omega_c'$ is significantly higher than $a_T\omega_c''$ for both L10 and S10.[2−5,8]

The application of time−temperature superposition to thermorheologically complex liquids such as block copolymers deserves some comment, given that there are two temperature-dependent monomeric friction coefficients in the system (corresponding to the PS and PI rich microdomains respectively) and the morphology is itself temperature dependent.[31,32] First, although there are two monomeric friction coefficients in the PS−PI copolymers, the relaxation time scales of the PI and PS domains are very different (due to their widely differing glass transition temperatures T_g) so that depending on the frequency range probed, the data may

be time−temperature superposable using shift factors based on one domain or the other over a limited frequency range. Using the Rouse frequency (eq 6) of equivalent homopolymer chains as an estimate for the terminal single chain relaxation frequency for the PI and PS blocks in L10, S10, we find $\omega_R^{PI} \approx 3 \times 10^7$ rad/s and $\omega_R^{PS} \approx 700$ rad/s (at T_0). This means that within the experimental frequency range studied in figs. 6a and b, we are effectively measuring the relaxation spectra due to PS domains alone.[45] From Figure 7, we note however that the temperature dependence of a_T for both L10 and S10 is not that of pure PS but is intermediate between PS and PI. This is probably because for our low molecular weight samples, the segregation between monomers is not very strong, so that there is a substantial concentration of PI monomers even within the PS rich domain and vice versa.[46]

Second, although the morphology of L10 and S10 changes going through the ODT, for these low molecular weight symmetric samples, composition fluctuations are important near the ODT;[23] these tend to smear out the morphological changes between the ordered lamellar phase and the disordered phase going through the ODT. This may explain why applying time−temperature superposition over the limited temperature range around T_{ODT} in L10 and S10 appears to produce well-defined master curves at high frequencies as well as physically sensible horizontal shift factors a_T. For the higher molecular weight samples L20, S20, L60, and S60, we are well into the ordered phase regime where there is relatively little morphological change over the temperature range studied. Time−temperature superposition is therefore possibly applicable for these higher molecular weight systems as well.

We note that for the linear system, the critical frequencies ω_c', ω_c'' are significantly higher than for the stars, $\omega_c'(L10)/\omega_c'(S10) \approx 25$, $\omega_c'(L10)/\omega_c''(S10) \approx 20$. This is rather surprising given that one normally thinks of ω_c to be a characteristic of the mesophase structure, independent of molecular architecture. Indeed previous measurements on homologous pairs of symmetric diblocks and triblocks have found ω_c for the diblocks and triblocks to be very close to one another: for example for poly(ethylenepropylene)−poly(ethylethylene) (PEP−PEE), Gehlsen et al.[5] have found $\omega_c(diblock)/\omega_c(triblock) \approx 1$ while for PS−PI, Riise et al.[9] have found $\omega_c(diblock)/\omega_c(triblock) \approx 3$, when the rheological data were shifted to a common reference temperature. We offer an explanation for the difference in ω_c between diblocks vs A_2B_2 stars in terms of the layer hopping time of block copolymers.

For many diblock systems, it has been found that the first deviation from homopolymer viscoelastic response, which might be called some kind of inverse longest chain relaxation time or critical frequency ω_c, corresponds very well to the time to diffuse through the layers by one layer spacing.[37] We shall assume this to be true for block copolymers with other architectures as well, including ABA triblocks, A_2B_2 four-arm stars, etc. When considering the layer diffusion time for ABA triblocks, however, it is necessary to distinguish "complete hopping", i.e., where the central B block moves to the adjacent B layer so that the whole chain moves by one period along the lamellar structure, from just "block escape", i.e., where one A block pulls into the adjacent A layer while the other A block and the B block remain in the original A and B layer, respectively. We expect the "block escape"

time to be comparable to the layer diffusion time of an AB diblock but much faster than "complete hopping" since "complete hopping" incurs a much higher energy penalty compared to "block escape" (the B block is twice as long as the A block for symmetric ABA). On the other hand, "block escape" is not possible for A_2B_2 stars, so that layer diffusion has to proceed via "complete hopping"; this is much slower than the layer diffusion of the homologous diblock because star diffusion incurs twice the energy penalty of diblocks (i.e., $2\chi N_{diblock}$ instead of $\chi N_{diblock}$, where $N_{diblock}$ is the polymerization number of the diblock). Consequently, while the time scale for chain hopping between linears and triblocks could be quite similar, we expect the time scale for chain hopping to be much slower in stars compared to diblocks. This is in agreement with the experimental data for diblocks vs triblocks and diblocks vs stars.

Assuming that ω_c is correlated to the layer diffusion time of the chains, i.e., $\omega_c = D_{perp}/L^2$, we can try to estimate the difference between ω_c for L10 and S10 quantitatively as follows. Here D_{perp} is the self-diffusion constant of a lamellar block copolymer through the layers and L the lamellar domain spacing. From SAXS, at $T = 140$ °C, we find $L = 175$, 192 Å for L10 and S10 respectively (see Table 2). For diblocks, D_{perp} has been determined empirically for well entangled lamellar PEP−PEE diblocks by Lodge and Dalvi, and they find the relation $D_{perp}/D_0 = \exp\{-0.422(\chi N_{diblock} - 9.1)\}$, where D_0 is the diffusion constant in the absence of the energy barrier to diffusion.[38,39] Assuming that the barrier to diffusion through the layers is largely independent of the exact mechanism of motion, we shall apply this expression to our unentangled diblock material, L10. The diffusion constant for A_2B_2 stars can be estimated by modifying this expression to $D_{perp}/D_0 = \exp\{-0.422(2\chi N_{diblock} - 18.2)\}$ where the factor 2 in front of $\chi N_{diblock}$ in the exponent is due to the star having to drag two A blocks into a B layer and vice versa. We have also assumed that the value of $\chi N_{diblock}$ where the barrier vanishes remains the same as in the diblock case. This is probably reasonable since L10 and S10 are thermodynamically very similar (they are identical within mean-field theory).[22]

Using the parameter values given in Appendix A to calculate $N_{diblock}$ and χ given by eq 3, for $T = 140$ °C we find $\chi N_{diblock} = 15.8$ for both L10 and S10. This gives $D_{perp}(L10)/D_0(L10) = 5.9 \times 10^{-2}$ and $D_{perp}(S10)/D_0(S10) = 3.5 \times 10^{-3}$. Now it is difficult to estimate the absolute value of $D_{perp}(L10)$ or $D_{perp}(S10)$ due to difficulties in estimating D_0 for PS−PI systems in the microphase separated state; as pointed out by Hamersky et al., one cannot simply use the value for D_0 in the disordered state because of the strong dependence of D_0 on the PS composition in the microdomains.[39] However, we can estimate the ratio of D_0 values which allows us to estimate the ratio of ω_c values. We expect $D_0(L10)/D_0(S10) = 2$, since at the same T for L10 and S10 (i.e., same $\chi N_{diblock}$), their microdomain compositions and therefore average friction coefficients are similar and, in addition, both materials are unentangled so that Rouse scaling should be obeyed. Combining all the above estimates for L, $D_\perp$, and D_0, we arrive at the final result $\omega_c(L10)/\omega_c(S10) \approx 40$. This compares favorably with the experimental results of $\omega_c'(L10)/\omega_c'(S10) \approx 25$ and $\omega_c''(L10)/\omega_c''S(10) \approx 20$.

In the limit of very high frequency, the values of G'' for L10 and S10 appear to converge (the effect in G'
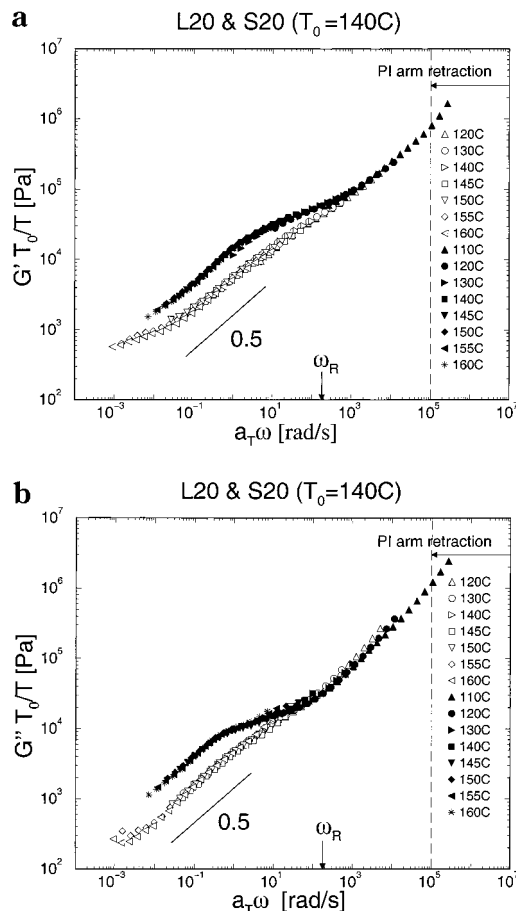

Figure 8. (a) Dynamic storage modulus and (b) dynamic loss modulus of L20 (unfilled) and S20 (filled) shifted to a reference temperature of $T_0 = 140$ °C. The frequency range for PI arm molecular relaxations (calculated from the Milner−McLeish model) and the Rouse frequency of the PS blocks are indicated.

is delayed to slightly higher frequencies). However, differences in G', G'' between S10 and L10 emerge for $\omega \gtrsim \omega_c$; specifically both G' and G'' for S10 exhibit a shoulder which is absent for L10. The additional shoulder in the star materials is even more striking for S20, we shall therefore delay discussion of this point until the next subsection. Finally, we note that the temperature dependence of a_T for S10 is closer to that of PS compared to L10 (see Figure 7). This is consistent with the fact that the T_{ODT} of S10 is significantly higher than that of L10 so that we would expect stronger phase segregation in S10 at the same temperature (below T_{ODT}). This is supported by the SAXS results which show the S10 chains to be more strongly stretched compared to L10 (see Table 2).

C. Rheology of L20 and S20. Figure 8a shows G' and Figure 8b shows G'' as a function of frequency ω for L20 (open symbols) and S20 (filled symbols). As before, the data have been subjected to time−temperature shifting both vertically and horizontally in order to superpose the high-frequency part of G''; this produced good superposition in G' and G'' over almost the entire frequency range. The horizontal shift factors a_T for L20 and S20 were found to fit the WLF equation well and both a_T and the best fit WLF curves are shown in Figure 7 (c_1, c_2 are listed in Table 2). We note that the shift factors for L20 and S20 are very close to that of pure PS, suggesting that the high-frequency part of

the rheology is due to PS chain relaxations. We can estimate the terminal PS chain relaxation frequency from the Rouse frequency since the PS block weights in both L20 and S20 are below the entanglement threshold (M_c). Using eq 6 and the parameters in Appendix A, we find the Rouse frequency of the PS block to be $\omega_R \equiv 1/\tau_R \approx 180$ rad/s; this is within the experimental frequency range and therefore supports the fact that the high-frequency part of the L20 and S20 rheology is due to PS chain relaxations. Although the PI chains are more entangled than the PS chains, its much lower T_g results in much faster relaxation times compared to PS. The terminal relaxation time of the PI chains can be estimated by exploiting the similarity of the entangled PI block dynamics to "arm retraction" dynamics in homopolymer stars, due to the thermodynamic pinning of the PS−PI block junctions. Using the parameter-free theory of Milner−McLeish for homopolymer stars (see Appendix B)[14,15] and the PI parameters given in Appendix A, the terminal time of PI chains is estimated to be $\omega_{term}^{PI} \equiv 1/\tau_{term}^{PI} = 10^5$ rad/s. Clearly, the PI chains relax much faster than the PS chains so that, on experimental time scales, the dominant contribution to the molecular viscoelasticity comes from the PS chains.

For $\omega \gg \omega_R$, the L20 and S20 data coincide and exhibit Rouse scaling of G', $G' \sim \omega^{1/2}$. This is what we would expect since the high-frequency G', $G' \sim \omega^{1/2}$ Rouse modes are insensitive to molecular architecture. For $\omega \ll \omega_R$, both the L20 and S20 data exhibit nonclassical terminal scaling of G', $G' \sim \omega^{1/2}$; we identify these as being due to deformations of the lamellar microdomains. Because of the higher molecular weight of L20 and S20 compared to L10 and S10, the disordered phase could not be accessed because the T_{ODT} was too high. Classical terminal scaling was therefore not observed even at the highest temperatures. We note that the low ω data for L20 and S20 do not coincide, with the S20 data being shifted to lower frequency. This indicates that the critical frequency for the onset of mesophase relaxations ω_c occurs at a lower frequency for S20. At the lowest frequencies, there appears to be some additional slow modes in the L20 rheology. Similar low-frequency processes were observed in a previous study[11] and are probably due to the relaxation of large scale grain domains in the sample.

While the L20 and S20 data coincide for $\omega \gg \omega_R$, differences emerge for $\omega \approx \omega_R$. Specifically, both G' and G' for S20 exhibit a shoulder which is absent for L20. This shoulder was also observed in S10 but is more striking for S20. There are two possible mechanisms giving rise to this shoulder: 1. The different molecular architectures of L20 and S20 give rise to differences in the terminal Rouse spectra; 2. The lower ω_c in S20 leads to a slower relaxation of the stress carried by mesophase deformations. We shall explore these two models in turn and evaluate their validity by seeking to fit quantitatively the L20 and S20 experimental data.

1. Differences in the Terminal Rouse Spectrum. While the high frequency Rouse modes of different polymer chains are insensitive to differences in molecular architecture, we expect differences in molecular topology to be reflected around the terminal regime of the Rouse spectrum. Referring to Figure 9, due to more severe thermodynamic and topological constraints acting on S20 compared to L20, one might expect the fluctuations of the block junction normal to the interface
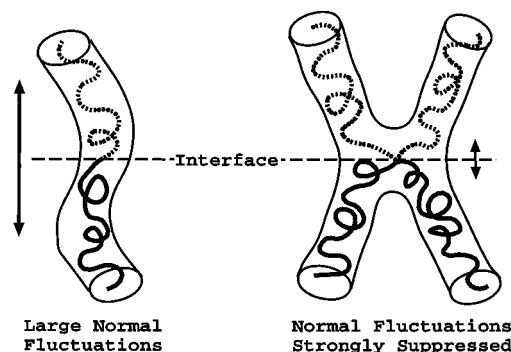

Figure 9. Combination of thermodynamic constraints at the interface between PI-rich and PS-rich domains and topological constraints (i.e., tube potential) restricting the perpendicular block junction fluctuations of hetero-stars more than linear diblocks.

between PS and PI rich domains to be more strongly suppressed in S20 compared to L20. The greater thermodynamic constraints in S20 come from the fact that normal fluctuations of the block junction in S20 involves dragging twice as many monomers into "enemy" territory compared to L20. The greater topological constraints are due to the PI chains in L20 and S20 being entangled, so that there is a "tube" potential acting on the PI chains which restricts motion lateral to the tube; while normal fluctuations of the L20 block junction can presumably proceed via (activated) reptation in the tube, this is suppressed for S20 due to the presence of the star branch point. The sum total of these two effects therefore may lead to a stronger degree of block junction pinning normal to the interface in S20 compared to L20. (There should also be a difference in the mobility along the interface between the two polymers. However, according to the theory of Rubinstein on homopolymer star diffusion, the difference probably only involves a combinatorial prefactor and is therefore not very great.[40]) Given that on time scales of interest, the PI blocks are essentially completely relaxed, we shall assume, to a first approximation, that we can model the Rouse modes of PS blocks in L20 and S20 (normal to the interface) as that of a free and tethered chain, respectively. For simplicity, we shall also neglect the effect of the chemical potential field which is present in block copolymers to maintain the composition profile of the mesophase structure. We expect that inclusion of this field does not alter the qualitative features of the Rouse spectrum though it may lower the absolute frequency scale. The Rouse modes for a free and tethered chain can be most easily derived pictorially by considering the normal modes of a fixed length of chain which have either a node or an anti-node at the chain ends depending on the boundary conditions (Figure 10). Noting that the relaxation time of a mode is proportional to the square of the wavelength, it is then easy to see that for a free chain, the spectrum of relaxation times is

$$\tau_p = \tau_R/p^2; \quad p = 1, 2, 3, \ldots \quad (4)$$

while for a tethered chain, it is

$$\tau_p = 4\tau_R/(2p-1)^2; \quad p = 1, 2, 3, \ldots \quad (5)$$

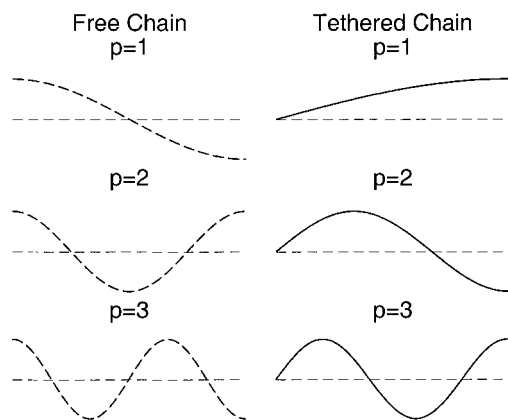where τ_R is the longest viscoelastic (as opposed to

Figure 10. Displacement as a function of length along chain for the first three Rouse modes ($p = 1, 2, 3$) of a free chain (dashed line) and tethered chain (solid line) of equal length.

rotational) Rouse relaxation time for a free chain and is theoretically predicted to be[41]

$$\tau_R = \frac{\zeta N^2 b^2}{6\pi^2 k_B T} \qquad (6)$$

where ζ is the monomeric friction coefficient, N the number of monomers in a PS block, b the statistical segment length, k_B is the Boltzmann constant, and T is the absolute temperature. We note that, for the tethered chain, the relaxation time of the fundamental mode ($p = 1$) is four times longer compared to the free chain. In addition, the relaxation time of the $p = 1$ mode is 9 times longer than the $p = 2$ mode while for the free chain, $p = 1$ is only 4 times longer than $p = 2$. The combination of the lower frequency of the fundamental Rouse mode and the larger spacing between the $p = 1$ and $p = 2$ Rouse modes in the tethered chain give rise to an additional shoulder in G' and G'' which is qualitatively similar to that observed in the S20 data (see Figure 11, parts a and b).

The storage and loss modulus due to these Rouse modes are given by[41]

$$G'_R(\omega) = \frac{1}{2} G_0 \left(\frac{N_e}{N}\right) \sum_{p=1}^{\infty} \frac{(\omega\tau_p)^2}{1 + (\omega\tau_p)^2} \qquad (7)$$

$$G''_R(\omega) = \frac{1}{2} G_0 \left(\frac{N_e}{N}\right) \sum_{p=1}^{\infty} \frac{\omega\tau_p}{1 + (\omega\tau_p)^2} \qquad (8)$$

where G_0 is the Plateau modulus of PS, N is the length of the PS block (i.e., the number of monomers), N_e the entanglement length and the prefactor of $1/2$ in eqs 7 and 8 accounts for the fact that shear stress is carried by only half the bulk material, namely the PS domains, since the PI domains have completely relaxed on experimental time scales.

To quantitatively evaluate the model that we have presented above, we have fitted by hand the G'' data for L20 and S20 with eqs 8 and 4 and eqs 8 and 5, respectively. In fitting the data, we used for N_e the PS homopolymer value given in Appendix A and left G_0 and $\omega_R \equiv 1/\tau_R$ as free fitting parameters. The best fits were obtained for the parameter values $G_0 = 6 \times 10^4$ Pa and $\omega_R = 120$ rad/s and in Figure 11, parts a and b, the G' and G'' data together with the best fit curves are plotted.
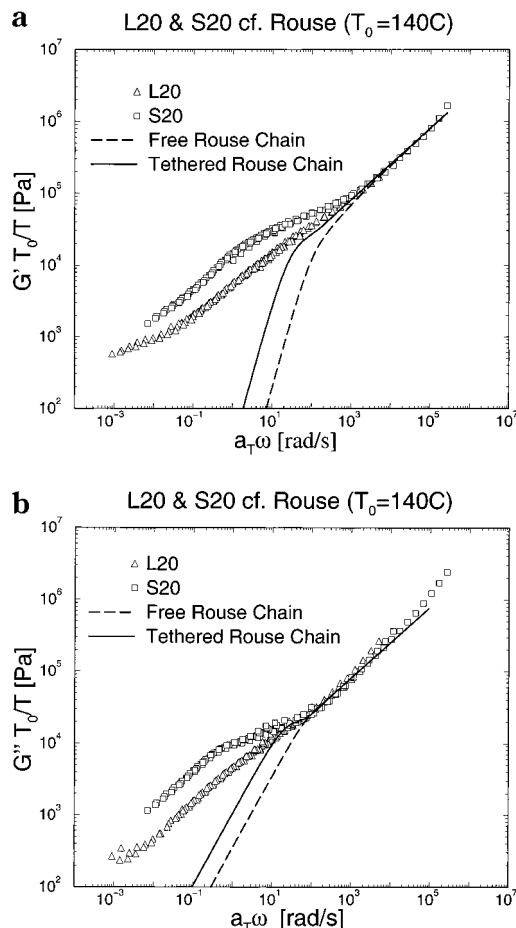

Figure 11. (a) Dynamic storage modulus and (b) dynamic loss modulus of L20 (triangles) and S20 (squares) compared to the free (dashed line) and tethered (solid line) Rouse models for the PS block with the fitting parameters $\omega_R = 118$ rad/s, $G_0 = 6 \times 10^4$ Pa.

The values of the fitted parameters are physically reasonable: ω_R is in excellent agreement with the expected value of $\omega_R = 180$ rad/s predicted by eq 6; G_0 is only a factor of 3 lower than the experimental value of $G_0 = 2 \times 10^5$ Pa for PS homopolymers.[42] However while the model for the tethered chain gives rise to a shoulder in G' and G'' which is qualitatively similar to that observed in the S20 data, it clearly fails to capture the intermediate and low ω data: the predicted frequency range of the shoulder in G' and G'', and the modulus of the shoulder in G' is much smaller than in the experimental data. One shortcoming of the Rouse model we have presented is that we have not included the contribution from mesophase relaxations; consequently, our model exhibits classical terminal scaling rather the observed nonclassical terminal scaling of G', $G'' \sim \omega^{1/2}$. The large discrepancy between the Rouse model and the experimental data suggests that the shoulder observed in the star system may be primarily due to differences in the mesophase relaxation between L20 and S20 rather than differences in the terminal Rouse spectrum. In the next part, we therefore incorporate mesophase relaxations into our model.

2. Effect of Differences in Mesophase Dynamics. A second possible mechanism giving rise to the shoulder in the star material is that S20 possesses a higher mesophase relaxation modulus and/or slower mesophase relaxations compared to L20. Including the mesophase
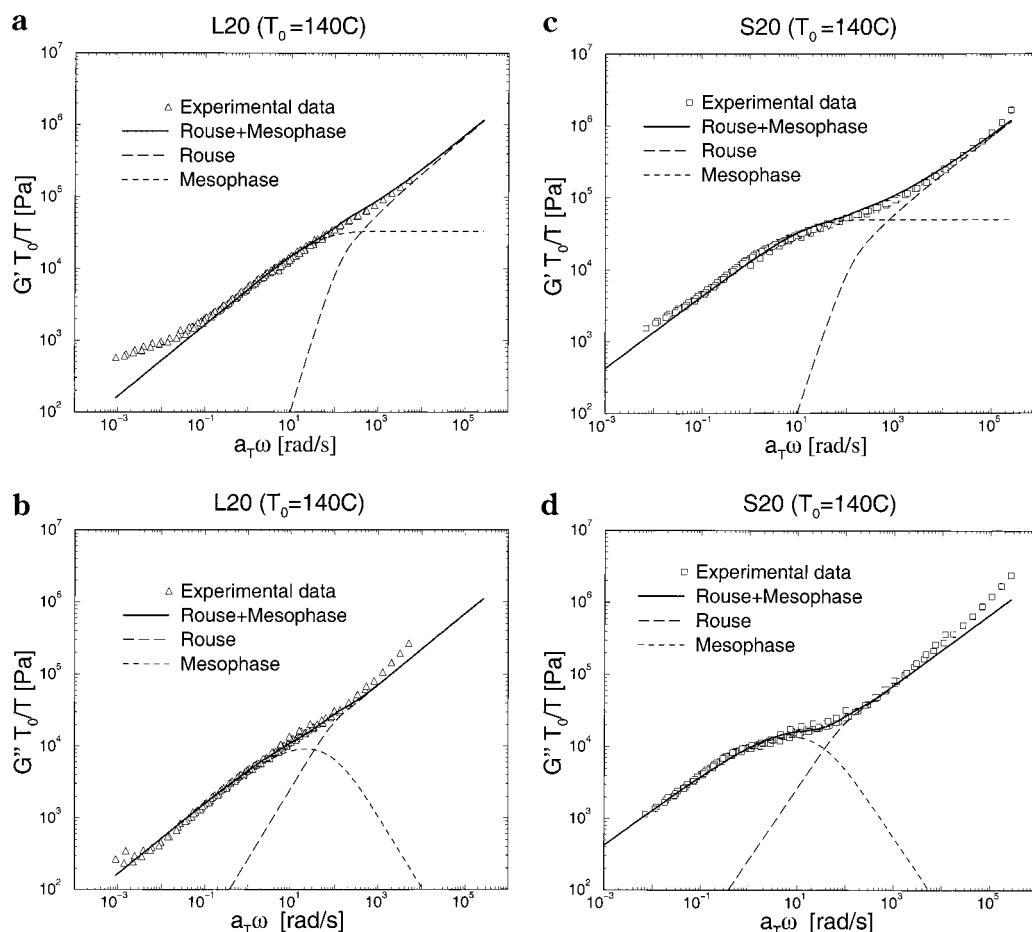
Figure 12. (a) Dynamic storage modulus and (b) dynamic loss modulus of L20 compared to the free Rouse + mesophase model with fitting parameters $\omega_R = 155$ rad/s, $G_0 = 6 \times 10^4$ Pa, $\omega_c = 64$ rad/s, and $G_{M0} = 3.3 \times 10^4$ Pa. (c) Dynamic storage modulus and (d) dynamic loss modulus of S20 compared to the free Rouse+mesophase model with fitting parameters $\omega_R = 155$ rad/s, $G_0 = 6 \times 10^4$ Pa, $\omega_c = 22$ rad/s, and $G_{M0} = 5 \times 10^4$ Pa; in each case, the Rouse and mesophase contributions are also plotted out (long dashed and dashed lines respectively).

contribution to the Rouse spectrum, the expressions for G' and G'' are modified to

$$G'(\omega) = G'_R(\omega) + G'_M(\omega) \qquad (9)$$

$$G''(\omega) = G''_R(\omega) + G''_M(\omega) \qquad (10)$$

Here G'_R and G''_R are the Rouse contributions to G' and G'' respectively and are given by eqs 7 and 8, respectively. For both L20 and S20, the free chain Rouse spectrum (i.e., eq 4) was used because we found that good fits to either the S20 or L20 data could not be obtained using the tethered chain Rouse spectrum (i.e., eq 5). The modulus G'_M and G''_M represent the mesophase contributions to G' and G'' respectively. In the time domain, this is modeled by the phenomenological expression

$$G_M(t) = \frac{G_{M0}}{(1 + t/\tau_c)^{1/2}} \qquad (11)$$

where G_{M0} is the modulus due to the deformation of microdomains and $\omega_c \equiv 1/\tau_c$ is the critical frequency for the onset of mesophase relaxations. Equation 11 represents the simplest expression that gives correct asymptotic behavior at both short and long times: for $t \ll \tau_c$, $G(t) = G_{M0}$; i.e., the mesophase stress remains unrelaxed, while for $t \gg \tau_c$, we obtain the correct

nonclassical terminal scaling of $G(t) = G_{M0}(t/\tau_c)^{-1/2}$. The response functions in the frequency domain, $G'_M(\omega)$ and $G''_M(\omega)$, are readily calculated by exploiting the inverse Laplace transform of $G_M(t)$.

The L20 and S20 data were fitted using the above model as follows. We first fitted by hand the G'' data for S20 using eq (10), with $G''_R(\omega)$ given by eqs 8 and 4, $G''_M(\omega)$ given by (the Fourier−Laplace transform of) eq 11 and leaving G_0, ω_R, G_{M0}, and ω_c as free fitting parameters. The best fit was obtained for the parameter values $G_0 = 6 \times 10^4$ Pa, $\omega_R = 155$ rad/s, $G_{M0} = 5 \times 10^4$ Pa, and $\omega_c = 22$ rad/s. The L20 data were then fitted keeping G_0 and ω_R fixed at the S20 values and using G_{M0} and ω_c as free parameters. The best fit was obtained for $G_{M0} = 3.3 \times 10^4$ Pa and $\omega_c = 64$ rad/s. The rationale for keeping G_0 and ω_R fixed is the fact that the L20 and S20 data coincide at high ω. In Figure 12, parts a and b, we plot the L20 G' and G'' data respectively together with the best fit curves while in Figure 12, parts c and d we plot the S20 G' and G'' data respectively together with the best fit curves.

The model including mesophase relaxations produces remarkably good fits to both the L20 and S20 data, with physically reasonable fitting parameters (the slight deviations from the Rouse model in the high ω G'' data are probably due to interference from high-frequency PS glassy dynamics). The fitted value of G_0 is only a factor of 3 lower than the value for PS homopolymers $G_0 = 2 \times 10^5$ Pa.[42] The lower G_0 is probably due to the

fact that the PS and PI single chain relaxations are not strictly independent but are coupled via relaxations of the microdomains (see subsection III.D). The stress carried by PS chain deformations after the PI chains have relaxed may therefore be significantly less than half the total stress, which was assumed in our model. The fitted value for ω_R is in good agreement with the value of $\omega_R = 90$ rad/s predicted by eq 6. The fitted values of G_{M0} for L20 and S20 are within 50% of each other while the fitted value of ω_c for S20 is a factor of 3 lower than for L20. Both G_{M0} and ω_c values for L20 and S20 are in good agreement with the predictions of Kawasaki−Onuki theory (see later).[43] From the fact that quantitative fits to the L20 and S20 data can only be obtained if one includes the mesophase contribution and uses the free chain Rouse spectrum, we conclude that the additional shoulder in S20 (and probably S10) is primarily due to differences in the mesophase relaxations between the linear and star materials rather than differences in the Rouse terminal spectra (at least within the framework of our model).

We note that ω_c for the star material (S20) is smaller than the linear material (L20), though the difference between L20 and S20 is much smaller compared to that between L10 and S10. Estimating the layer diffusion time for L20 and S20 chains using the same method as in subsection III.B (assuming PS frictional coefficients for the whole chain), we find values for the inverse layer diffusion time which are many orders of magnitude smaller than ω_c. In addition, the inverse layer diffusion time for S20 is found to be many orders of magnitude smaller than for L20, which again does not agree with the difference in the fitted values of ω_c that we find. This suggests that, for higher molecular weight block copolymers that are more strongly segregated, the layer diffusion time becomes so slow that the system may choose alternative routes for mesophase stress relaxation. One such alternative is for the system to relax via collective hydrodynamic fluctuations of the lamellar layers, as envisaged in the Kawasaki and Onuki theory for block copolymer mesophase relaxation.[43] The theory predicts $G_{M0} \approx 0.1\ B$ and $\omega_c = B/\eta$, where B is the compression modulus of the lamellar layers and η is the appropriate viscosity associated with the mesostructure, which in this case is the viscosity of the PS layers (see subsection III D for more details). We can estimate B for L20 and S20 lamellar layers by scaling down typical values of B for small molecule smectics, $B_s \approx 6 \times 10^6$ Pa.[43] Using scaling arguments which are valid in the strong segregation regime, it can be easily shown that $B/B_s \approx \lambda_s/\lambda$, where $\lambda_s \approx 10^{-9}$ m is the typical lamellar spacing in small molecule smectics and λ is the lamellar spacing in L20 or S20. From SAXS, $\lambda = 2\pi/q^* \approx 300$ Å, so that $B \approx 2 \times 10^5$ Pa. The viscosity of the PS layer η can be estimated from $\eta \approx G_0(N_e/N)\tau_R$, where G_0 and N_e are respectively the plateau modulus and entanglement length of PS, N, and τ_R are respectively the length and rouse time of the PS block. Using the parameter values given in Appendix A, we find $\eta \approx 2000$ Pa·s. Kawasaki−Onuki theory therefore predicts $G_{M0} \approx 2 \times 10^4$ Pa and $\omega_c = 100$ rad/s; This compares very favorably indeed with the fitted values of $G_{M0} = 3.3 \times 10^4$ Pa, $\omega_c = 64$ rad/s for L20 and $G_{M0} = 5 \times 10^4$ Pa, $\omega_c = 22$ rad/s for S20 and suggests that the mesophase dynamics of L20 and S20 are controlled by collective hydrodynamic layer fluctuations.

The smaller value of ω_c for S20 compared to L20 may be due to two factors. First, there is a stronger chemical potential field acting on the PS chains in S20 due to the stronger degree of microphase segregation in S20 (as shown by the stronger chain stretching observed from SAXS; see Table 2). This chemical potential field has hitherto been neglected in our discussion and results in slower PS chain relaxations in S20 compared to L20. Second, the stronger microphase segregation in S20 also results in the PS rich domains having a higher composition of PS. As shown by Hamersky et al., the effective friction coefficient of the PS rich domains in PS−PI copolymers is very sensitive to the PS composition;[39] the higher PS composition in S20 therefore leads to a higher effective friction coefficient which further slows down PS chain relaxation. This point is supported by the fact that the horizontal shift factors a_T for S20 is closer to pure PS compared to L20 (see Figure 7). Assuming that the Kawasaki−Onuki theory correctly describes the mesophase dynamics in L20 and S20, these two factors have the effect of increasing the PS layer viscosity η and therefore lowering ω_c in S20 compared to L20.

D. Rheology of L60 and S60. Parts a−d of Figure 13 show the rheology data for L60 (open symbols) and S60 (filled symbols). The data were subjected to vertical time−temperature shifting in the usual way. The horizontal shifting however was performed in two different ways. In Figure 13, parts a and b, the data were shifted to superpose the high frequency G'' data as before. This produced shift factors that were very close to that of pure PI (see Figure 7). Indeed, for S60, pure PI shifts were used to superpose the high-frequency data. We observe that the values of G'' for L60 and S60 appear to merge at high frequencies and converge for G''. Both L60 and S60 appear to exhibit G', $G'' \sim \omega^{1/2}$ behavior at high frequency, though this is better developed for L60 compared to S60. In Figure 13, parts c and d, on the other hand, horizontal shifting was performed using pure PS shift factors and these were found to superpose the low-frequency data of both L60 and S60 very well. At the lowest frequency, both G' and G'' again exhibit $\omega^{1/2}$ scaling, though the relaxation of S60 appears to be slower than L60 so that the data for L60 and S60 do not coincide at low frequency. Between the $\omega^{1/2}$ scaling at high and low frequencies, a relatively clear plateau is observed, which is presumably due to molecular entanglements. This is confirmed by calculation of the PS single-chain relaxation time (see Figure 13c). The interesting superposition behavior of L60 and S60 indicates that two distinct relaxation mechanisms are in operation at the high and low-frequency end of the data, which are controlled by PI and PS friction coefficients, respectively. Time−temperature superposition however breaks down for intermediate frequencies due to interference between these two mechanisms.

Given the high molecular weight of the PS blocks, we expect the PS chains to be entangled for both L60 and S60. We can estimate the longest molecular relaxation time of the PS chains using the Milner−McLeish theory as before. This gives (using PS parameters given in Appendix A) $\omega_{term}^{PS} \equiv 1/\tau_{term}^{PS} = 0.2$ rad/s. Taking into account the experimental uncertainty in the ζ parameter and the fact that we have neglected the chemical potential field acting on the block copolymer chains, the agreement between the theoretical estimate and the experimental value for the terminal frequency of the
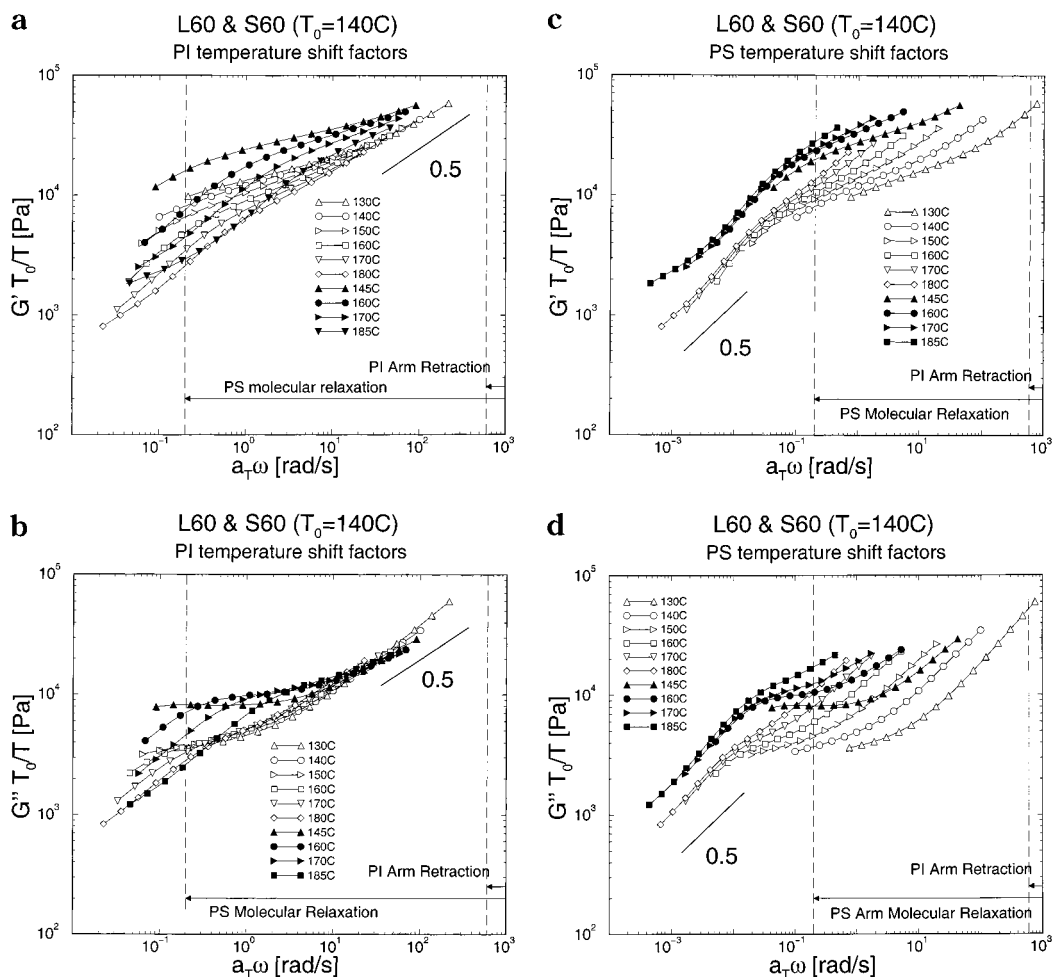
Figure 13. (a) Dynamic storage modulus and (b) dynamic loss modulus of L60 (unfilled) and S60 (filled) shifted to a reference temperature of $T_0 = 140$ °C. The data have been shifted to superpose the high-frequency part of the data. Pure PI shift factors have been applied to S60 while shift factors close to that of pure PI have been applied to L60 (see Figure 7). (c) Dynamic storage modulus and (d) dynamic loss modulus of L60 (unfilled) and S60 (filled) shifted to a reference temperature of $T_0 = 140$ °C using pure PS shift factors. The PS shift factors superpose the low-frequency part of the data very well. In parts a–d, the frequency range for PI and PS arm molecular relaxations calculated from the Milner–McLeish model are indicated.

plateau regime is reasonably good (the experimental value is ≈ 0.02 rad/s for both L60 and S60 from the point at which G' and G'' in parts c and d of Figure 13, respectively, first coincide). The terminal frequency of the PI chains on the other hand is estimated from the Milner–McLeish theory to be $\omega_{\text{term}}^{\text{PI}} \equiv 1/\tau_{\text{term}}^{\text{PI}} = 600$ rad/s which is much higher than the experimental terminal frequency of the plateau regime. We therefore identify the plateau as being due to PS entanglements. Below the terminal frequency of the plateau, we observe G', $G'' \sim \omega^{1/2}$ scaling rather than classical terminal scaling due to the presence of unoriented lamellar mesophase.

While the theoretical estimate of the PS terminal frequency is in reasonably good agreement with the plateau terminal frequency, the plateau moduli of L60 and S60 are rather low: about 10^4 Pa for S60 and less than 10^4 Pa for L60. This compares with an expected plateau modulus of $^1/_2 G_0(\text{PS}) \approx 10^5$ Pa for PS entanglements, where $G_0(\text{PS})$ is the modulus for bulk PS, and $^1/_2$ accounts for the fact that only half the volume of L60 and S60 consists of PS. The interpretation of the $\omega^{1/2}$ scaling at high frequency is at first sight equally puzzling. Given that the data superpose according to PI shift factors, naively, one might assume that the rheology arises from PI molecular relaxations. However,

as we have estimated earlier, the terminal frequency for PI single-chain relaxations is above the experimental frequency range ($\omega_{\text{term}}^{\text{PI}} \equiv 1/\tau_{\text{term}}^{\text{PI}} = 600$ rad/s). This means that the PI superposed region in Figure 13, parts a and b is deep into the PI terminal regime, where the modulus from PI molecular relaxations is much lower than the observed values and also obeys classical terminal scaling rather than the observed G', $G'' \sim \omega^{1/2}$ scaling.

The frequency and modulus scale of the PI superposed regime instead suggest that the underlying relaxation mechanism may be due to mesophase deformations rather than PI molecular relaxations. The different contributions to the total stress can be most easily understood by considering the linear response of the block copolymer system to a step strain in the time domain. The free energy density of the system immediately after the step strain is given by (assuming incompressibility)[43]

$$f = G_{\text{PI}}\left(\frac{1}{2}[\nabla\mathbf{u}^{\text{PI}} + (\nabla\mathbf{u}^{\text{PI}})^T]\right)^2 +$$
$$G_{\text{PS}}\left(\frac{1}{2}[\nabla\mathbf{u}^{\text{PS}} + (\nabla\mathbf{u}^{\text{PS}})^T]\right)^2 +$$
$$\frac{1}{2}B(\nabla_{\|}u_{\|})^2 + \frac{1}{2}K(\nabla^2_{\perp}u_{\|})^2 \quad (12)$$

where G_{PI} and G_{PS} are the appropriate elastic shear moduli for the PI and PS phase, respectively, B is the layer compression modulus and K is the bending modulus of the lamellar mesostructure, $\mathbf{u}^{PI}$ and $\mathbf{u}^{PI}$ are the displacament vectors due to deformation in the PI and PS phase respectively, $u_{\parallel}$ is the component of the displacement vector parallel to the local lamellar normal, $\nabla_{\parallel}$ and $\nabla_{\perp}$ are respectively the components of the ∇ operator parallel and perpendicular to the local lamellar normal, and $(\nabla\mathbf{u})^T$ is the transpose of the tensor $\nabla\mathbf{u}$. The first two terms in eq 12 represent contributions to the total stress arising from molecular deformations while the last two terms represent the contribution from mesophase deformations (in writing the last two terms, we have used the fact that the lamellar phase in block copolymers has the symmetry of the smectic A phase in liquid crystals.[43]) After the step strain, the different stress contributions decay with time at different rates from each other (the different relaxation processes however may not be independent of each other, as we shall see later). In most studies of block copolymer rheology, one assumes that the stress carried by mesophase deformations relaxes only after the molecular stress in both phases has effectively completely relaxed. However, for systems where there is a wide separation of glass transition temperatures (T_g) between the two microphases (e.g., PS−PI block copolymers), the molecular relaxation of the slower phase (i.e., the phase with higher T_g) may be pre-empted by a partial relaxation of the mesophase stress as we shall now demonstrate.

Within the frequency range of the PI superposed region, the PS phase behaves like a rubbery solid while PI phase-like a liquid, since $\omega^{PS}_{term} < \omega < \omega^{PI}_{term} \ll \omega^{PS}_{kuhn}$, where $\omega^{PS}_{term} \approx 0.2$ rad/s is the terminal frequency of the PS chains, $\omega^{PI}_{term} \approx 600$ rad/s is the terminal frequency of the PI chains and $\omega^{PS}_{kuhn} = 3\pi^2 k_B T/(\zeta b^2) \approx 3 \times 10^6$ rad/s is the Rouse frequency of a PS statistical segment length. The melting of one of the phases in the lamellar structure (i.e., PI) means that part of the stress carried by the mesophase may be able to relax despite the fact that the PS phase remains a solid. The stress relaxation spectrum of a polydomain lamellar block copolymer has been calculated by Kawasaki and Onuki[43] by exploiting the identical symmetry of the lamellar mesophase to smectic A liquid crystals. Their result for G', G'' is

$$G'(\omega) \approx G''(\omega) \approx 0.1B\left(\frac{\omega}{\omega_c}\right)^{1/2} \qquad (13)$$

The frequency dependent rheology in this model is due to the hydrodynamic fluctuations of the lamellar layers and the theory applies at low frequency, $\omega < \omega_c$, where

$$\omega_c = B/\eta \qquad (14)$$

is the critical frequency for the onset of mesophase rheology. Here B is the lamellar compression modulus and η is an appropriate viscosity associated with the mesostructure.

Applying this theory to L60 and S60, it is clear that the appropriate viscosity in the frequency range of interest is the viscosity of the PI phase, i.e., $\eta = \eta_{PI} \approx G_0(PI)\tau^{PI}_{term} \approx 70$ Pa·s. The contribution of the PS phase to B can be estimated to be roughly the same as the rubber plateau modulus of PS $G_0(PS) \approx 2 \times 10^5$ Pa, since uniaxial compression is a volume preserving deformation. The contribution of the PI phase to B can
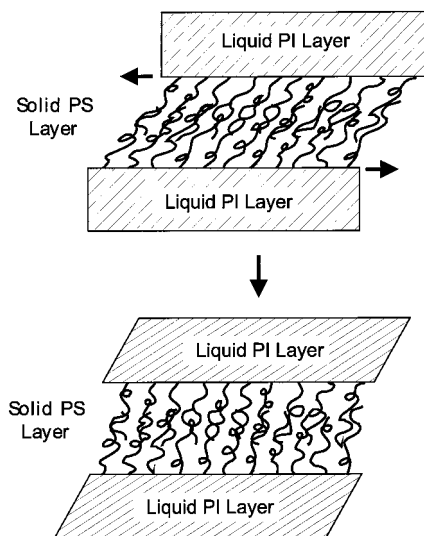

Figure 14. Illustration of how PI controlled mesophase relaxations can be coupled to PS molecular relaxations: the liquid nature of the PI layers means that the PS−PI interface on either side of the solid PS layer can be displaced with respect to each other, leading to a significant relaxation of stress in the solid PS layer.

be estimated from the free energy of compressing two polymer brush layers against each other. Using strong segregation theory, we get the scaling result $B \approx \chi^{1/3}N_{PI}^{-2/3}k_B T/v_{PI} \approx 10^5$ Pa. We can also estimate the contribution of PI to B by scaling down typical values of B for small molecule smectics, as discussed in subsection III.C. This gives $B \approx 10^5$ Pa, which is in good agreement with our first estimate. Interestingly, the contributions from PS and PI are nearly the same, we therefore set $B \approx 10^5$ Pa for the entire sample. Using these values of η and B, we find $\omega_c \approx 10^3$ rad/s. We note that $\omega_c \gg \omega^{PS}_{term}$ and $\omega_c \approx \omega^{PI}_{term}$. This means that, intermediate between the PI and PS single-chain terminal relaxation frequencies, we expect to find a PI rate controlled mesophase relaxation with G', $G'' \sim \omega^{1/2}$. This prediction is in both qualitative and quantitative agreement with the experimental data in Figure 13, parts a and b.

Although we have separated out the different contributions to the total stress in eq 12, it is important to realize that the relaxation mechanisms of these different contributions are not independent of each other. This is illustrated in Figure 14 where we show a solid PS layer sandwiched between two liquid PI layers. The liquid nature of the PI layers means that the PS−PI interface on either side of the PS layer can be displaced with respect to each other leading to a significant relaxation of the stress carried by the deformation of PS chains, even for $\omega_c \gg \omega^{PS}_{term}$. The coupling of PI controlled mesophase relaxations to PS molecular relaxations in this and analogous ways may explain why the PS entanglement plateau in Figure 13, parts a−d, is much lower than what we would expect for bulk homopolymers. For $\omega_c < \omega^{PS}_{term}$, we have melting of the PS phase also which allows the residual stress carried by mesophase deformations to be relaxed. The relevant viscosity for this process is the viscosity of the PS phase, η_{PS}. This leads to PS controlled $\omega^{1/2}$ scaling at low frequencies, as observed in Figure 13, parts c and d.

At this point, it is interesting to ask why the fast PI controlled mesophase relaxation described above was

not observed for L10, S10, L20, and S20 even though the condition $\omega_c \gg \omega_{term}^{PS}$ is also satisfied in those systems; e.g., for L20, S20, using the same theoretical estimates as above, we find $\omega_c \approx 5 \times 10^4$ rad/s while $\omega_{term}^{PS} \approx 100$ rad/s for L20 and S20. We offer the following heuristic argument based on the qualitatively different PS molecular relaxations in the higher and lower molecular weight block copolymer systems as a possible explaination for this anomaly. Let us consider the shear stress $\sigma(t)$, which represents the linear stress response (in the time domain) of the block copolymer system to a small step strain. For our system parameters (both high and low molecular weight samples), at $t = \tau_c^{PI} \equiv \eta_{PI}/B$, effectively all the PI molecular stress is relaxed, part of the PS molecular stress has already relaxed (via Rouse relaxation), while the mesophase stress is unrelaxed. Since the remaining PS stress is the dominant contribution to the overall stress, we can represent it by $\sigma_0 \equiv \sigma(\tau_c^{PI})$. For $t > \tau_c^{PI}$, relaxation of σ_0 can proceed via two possible routes:

i. PS molecular relaxation: for low molecular weight samples, the PS chains are unentangled or only marginally entangled, so that we have Rouse relaxation $\sigma(t) = \sigma_0(t/\tau_c^{PI})^{1/2}$; for L60, S60 however, the PS chains are entangled and the onset time of the plateau regime $\tau_e = \zeta b^2 N_e^2/(3\pi^2 k_B T) \approx 10^{-2}$ s is close to $\tau_c^{PI} \approx 10^{-3}$ rad/s. Therefore, for most of $\tau_c^{PI} < t < \tau_{term}^{PS}$, the stress remains unrelaxed, $\sigma(t) \approx \sigma(\tau_e)(t/\tau_e)^0$.

ii. PI controlled mesophase relaxation: as explained earlier, this can substantially relax PS molecular stress (see Figure 14). According to Kawasaki−Onuki theory,[43] this is approximately given by $\sigma(t) \approx \sigma_0(t/\tau_c^{PI})^{1/2}$ for both high and low molecular weight samples.

Assuming that we have parallel addition of relaxation modes, the system will always choose the faster relaxation route. For the lower molecular weight systems, PS molecular relaxation is at least as fast as PI controlled mesophase relaxation; there is therefore no need for the system to relax via PI controlled mesophase relaxation and it instead proceeds via normal PS molecular relaxation. For L60 and S60 however, PS molecular relaxations are much slower, especially in the plateau region $\tau_e < t < \tau_{term}^{PS}$; relaxation therefore proceeds via PI controlled mesophase relaxation.

If the above heuristic argument is correct, one would expect for $t > \tau_c^{PI}$ ($\omega < \omega_c^{PI}$), a crossover from PI dominated mesophase relaxations to PS molecular relaxations as τ_{term}^{PS} approaches τ_e from below. It would be interesting to study block copolymer samples with molecular weights between L20, S20 and L60, S60 to determine at what point this crossover in rheological behavior occurs.

Comparing parts a and b of Figure 13 with parts c and d of Figure 13, we note that the PI controlled $\omega^{1/2}$ relaxations coincide for the linear and star samples at high frequencies. However, differences between L60 and S60 emerge at the crossover between PI dominated and PS dominated dynamics; specifically, the relaxation of S60 appears to be slower compared to L60 in the plateau and PS controlled mesophase relaxation regions. This may be due to the stronger chemical potential field acting on the PS chains in S60, which leads to slower PS chain dynamics. It creates an *enthalpic* barrier to PS arm retraction of order $(\chi N)^{1/3}$ per chain,[44] in addition to the entropic barrier of order N/N_e per chain, where N is the number of monomers in the PS chain

(see Appendix B). The strength of this field is greater for S60 compared to L60 due to the stronger degree of phase segregation in S60 (as shown by the stronger chain stretching observed from SAXS, see Table 2). For PS chains, which are only moderately entangled ($N/N_e \approx 3.6$), the enthalpic barrier is comparable to the entropic barrier ($(\chi N)^{1/3} \approx 3.6$) so that the stronger chemical potential field leads to noticeably slower PS chain dynamics in S60 compared to L60. In contrast, this field does not appear to have an appreciable effect on PI chain dynamics, presumably because the PI chains are much more strongly entangled ($N/N_e \approx 9$), so that the enthalpic barrier is negligible compared to the entropic barrier.

IV. Conclusions

In this paper, we have studied the linear shear rheology and small-angle X-ray scattering of three symmetric styrene−isoprene (PS−PI) diblock copolymers L10, L20, and L60 compared to their hetero-four-arm star counterparts S10, S20, and S60. The SAXS data showed that for both the linear and star systems, the first-order reflection peak q^* scaled with overall molecular weight N according to $q^* \sim N^{-\delta}$, with $\delta \approx 0.7$ for both linear and star systems. However, the star chains were consistently 5−10% more strongly stretched compared to their linear counterparts, indicating stronger phase segregation in the hetero-arm stars. This is consistent with rheological measurements of T_{ODT}, where we found the T_{ODT} of S10 to be significantly higher than L10: $T_{ODT} \approx 160$ °C for L10 and $T_{ODT} \approx 200$ °C for S10. The T_{ODT} values for L20, S20, L60, and S60 were much higher than the sample degradation temperature and therefore could not be accessed experimentally.

Dynamic frequency sweep data were measured for all six block copolymer samples in the unoriented state and extremely rich rheological behavior was found. For L10, S10, the system is in the disordered phase for $T > T_{ODT}$ and the rheology exhibited classical terminal behavior at low frequency, i.e., $G' \sim \omega^2$, $G'' \sim \omega$. For $T < T_{ODT}$, nonclassical terminal behavior with the approximate scaling G', $G'' \sim \omega^{1/2}$ was observed at low frequencies due to the formation of the lamellar mesophase, while single chain relaxations dominated at high frequencies with the data being time−temperature superposable. The critical frequency for mesophase relaxations ω_c was determined by the intersection of the disordered branch with the main branch of the rheology. We found ω_c for S10 to be about 20 times smaller compared to L10 when the data were time−temperature superposed to a common reference temperature. This correlated very well with quantitative estimates of the difference in lamellar hopping time between L10 and S10 and suggests that mesophase relaxations for the 10K arm block copolymers may be controlled by layer hopping of chains.

For L10, S10, L20, S20, the high-frequency part of the rheology data could be superposed with shift factors close to that of pure PS, indicating that PS chain relaxations dominate for $\omega \gg \omega_{term}^{PS}$, where ω_{term}^{PS} is the PS block terminal relaxation frequency. For $\omega \ll \omega_{term}^{PS}$, mesophase relaxations dominate and nonclassical terminal scaling of G', $G'' \sim \omega^{1/2}$ was observed. No PI molecular relaxation was observed as the inverse longest PI chain relaxation time was above the experimental frequency. For L10, S10, L20, and S20, the rheology of the linear and star analogues coincide

for $\omega \gg \omega_{\text{term}}^{\text{PS}}$, but an additional shoulder in G' and G'' emerges for the stars for $\omega \approx \omega_{\text{term}}^{\text{PS}}$. Excellent quantitative fits across the whole frequency range were obtained by fitting the L20 and S20 data to a simple model incorporating free chain Rouse dynamics and mesophase relaxations. Mesophase relaxations were found to be dominant in the shoulder region of S20; ω_c for S20 was found to be 3 times lower than in L20 while G_{M0} for S20 was only slightly higher than in L20. From our model fit, we therefore conclude that the shoulder observed in the star materials is a result of differences in the linear and star mesophase relaxations rather than differences in linear and star terminal Rouse modes. The resultant fitting parameters from the model were physically sensible, and in particular the critical frequency ω_c and mesophase modulus G_{M0} for L20 and S20 were found to be in good agreement with values predicted by Kawasaki–Onuki theory. In contrast, estimates for the inverse chain hopping time for L20 and S20 were many orders of magnitude lower than the fitted values of ω_c, with the inverse chain hopping time for S20 being many orders of magnitude lower than S20. This suggests a qualitative difference between the mesophase relaxations of the 10K and 20K arm materials, with the latter being controlled by collective hydrodynamic layer fluctuations rather than chain hopping events.

For L60 and S60, qualitatively different behavior from the lower molecular weight materials was observed. For $\omega < \omega_{\text{term}}^{\text{PS}}$, the terminal frequency of the PS chains, $\omega^{1/2}$ scaling was observed as expected (corresponding to mesophase relaxations) and the low-frequency data were found to be superposed using pure PS shift factors. However, for $\omega \gg \omega_{\text{term}}^{\text{PS}}$, the data were superposed by shift factors close to or equal to that of pure PI. The low modulus and frequency scales as well as the $\omega^{1/2}$ scaling at high ω however indicate that instead of PI molecular relaxations, we have PI controlled mesophase relaxations. We attribute this to the very fast relaxations of the PI chains so that even at the highest experimental frequencies, the PI phase has already melted, allowing the mesophase stress to partially relax. This is supported by theoretical estimates of the critical frequency for PI controlled mesophase relaxation ω_c^{PI}, where we find using Kawasaki–Onuki theory $\omega_c^{\text{PI}} \gg \omega_{\text{term}}^{\text{PS}}$. This is in striking contrast to block copolymers which only have a small difference in T_g between the two microphases, e.g.,, PEP–PEE, where ω_c is less than the longest chain relaxation time of both phases. We show that the PI controlled mesophase relaxation can also relax PS molecular stress and suggest that this is what leads to the unusually low PS entanglement modulus values observed for L60 and S60. For future work, we propose that the rheology of block copolymers with molecular weights between that of L20, S20 and L60, S60 should be studied to see at what point the crossover from PS molecular relaxations to PI controlled mesophase relaxations at high frequencies occurs. The rheology of L60 and S60 coincide for $\omega \gg \omega_{\text{term}}^{\text{PS}}$ but differences emerge for $\omega \gtrsim \omega_{\text{term}}^{\text{PS}}$. This difference is attributed to the stronger chemical potential field acting on the PS chains in S60 which leads to slower PS arm retraction dynamics.

In summary, our study has revealed interesting contrasting behavior between the rheology and lamellar spacings of linear (diblocks and triblocks) and star block copolymers, between the rheology of block copolymers with different degrees of segregation as well as between the rheology of block copolymers with more dissimilar blocks (in terms of T_g etc.), which have been used in this study, and block copolymers with more similar blocks studied by previous co-workers (e.g., PEP–PEE). Our study also allowed us to identify the underlying mechanisms responsible for the different regimes in block copolymer rheology, especially differentiating the single-chain relaxation regime from mesophase smectic viscoelasticity; these mechanisms would have been difficult to elucidate without employing the star and linear architectures and the wide range of molecular weights that have been used in this study.

Appendix A: Parameters for PI and PS chains

For the theoretical estimates performed in the paper, we have used the following parameters for PS and PI chains: for PI, $\zeta = 1.223 \times 10^{-12}$ N m^{-1} s, $b = 6.5$ Å, $\rho = 830$ kg/m^3 (i.e., $v = 1.36 \times 10^{-28}$ m^3, $c = 7.35 \times 10^{27}$ m^{-3}), and $M_e = 6786$ g/mol, while for PS, $\zeta = 1.12 \times 10^{-7}$ N m^{-1} s, $b = 6.7$ Å, $\rho = 969$ kg/m^3 (i.e., $v = 1.78 \times 10^{-28}$ m^3, $c = 5.61 \times 10^{27}$ m^{-3}), and $M_e = 16636$ g/mol where ζ is the monomeric friction coefficient, b and v are the monomer length and volume, respectively, ρ and c are the mass and number density, respectively, and M_e is the entanglement spacing. All results above are based on PI and PS homopolymer values with monomeric molecular weights of $M_0 = 68$ g/mol for PI and $M_0 = 104$ g/mol for PS and the results are referenced to $T = 140$ °C. The values for ζ are taken from Ferry[20] while all other parameters are taken from Fetters et al.[42] Note that our values for M_e are 1.25 times greater than in ref 42 in order to harmonize our definition of M_e with that of refs 14 and 15. For rheological calculations, the number of monomers in the PS and PI blocks are calculated using the PS and PI monomer weights respectively, i.e.

$$N_{\text{PS}} = M_n^{\text{PS}}/M_0^{\text{PS}}; \quad N_{\text{PI}} = M_n^{\text{PI}}/M_0^{\text{PI}}$$

where M_n^{PS} and M_n^{PI} are the number-averaged molecular weights of PS and PI blocks, respectively. On the other hand, for thermodynamic calculations, the total number of monomers in the block copolymer N (e.g., in $(\chi N)_{\text{ODT}}$) is calculated based on a common reference monomer volume $v = (v_{\text{PS}} v_{\text{PI}})^{1/2}$, i.e.

$$N = \frac{\dfrac{M_n^{\text{PS}}}{\rho_{\text{PS}}} + \dfrac{M_n^{\text{PI}}}{\rho_{\text{PI}}}}{\left(\dfrac{M_0^{\text{PS}}}{\rho_{\text{PS}}} \dfrac{M_0^{\text{PI}}}{\rho_{\text{PI}}}\right)^{1/2}}$$

Appendix B: Milner–McLeish Theory

The Milner–McLeish theory is a parameter-free theory that allows us to calculate the arm retraction time of entangled homopolymer star melts.[14,15] The relaxation time $\tau(s)$ for a star arm to retract a fractional

distance s ($0 < s < 1$, $s = 1$ at the star branch point) along its primitive path is given by[15]

$$\tau(s) = \frac{\tau_{early}(s)[U_{eff}(s)]}{1 + [U_{eff}(s)]\tau_{early}(s)/\tau_{late}(s)} \quad \text{(B1)}$$

where

$$\tau_{early}(s) = 225\pi^3/256\tau_e(N/N_e)^4 s^4 \quad \text{(B2)}$$

$$\tau_{late}(s) = \tau_e\left(\frac{N}{N_e}\right)^{3/2}\left(\frac{\pi^5}{30}\right)^{1/2} \times$$

$$\frac{\exp[U_{eff}(s)]}{s\left[(1-s)^{2\alpha} + \left\{\left(\frac{4N_e}{15N}\right)(1+\alpha)\right\}^{2\alpha/\alpha+1}\Gamma\left(\frac{1}{\alpha+1}\right)^{-2}\right]^{1/2}} \quad \text{(B3)}$$

$$U_{eff}(s) = \frac{15N}{4N_e}\frac{1 - (1-s)^{1+\alpha}[1 + (1+\alpha)s]}{(1+\alpha)(2+\alpha)} \quad \text{(B4)}$$

In the above equations, $\tau_e = \zeta N_e^2 b^2/(3\pi^2 k_B T)$ is the Rouse time for an entanglement length N_e, N is the length of the star arm (i.e., number of monomers in the arm), and α is the dilution exponent which we shall take as $\alpha = 7/3$ following Milner and McLeish.

References and Notes

(1) Zhao, J.; Majumdar, B.; Schulz, M. F.; Bates, F. S.; Almdal, K.; Mortensen, K.; Hajduk, D. A.; Gruner, S. M. *Macromolecules* **1996**, *29*, 1204.
(2) Bates, F. S. *Macromolecules* **1984**, *17*, 2607.
(3) Bates, F. S.; Rosedale, J. H.; Fredrickson, G. H. *J. Chem. Phys.* **1990**, *92*, 6255.
(4) Rosedale, J. H.; Bates, F. S. *Macromolecules* **1990**, *23*, 2329.
(5) Gehlsen, M. D.; Almdal, K.; Bates, F. S. *Macromolecules* **1992**, *25*, 939.
(6) Koppi, K. A.; Tirrell, M.; Bates, F. S.; Almdal, K.; Colby, R. H. *J. Phys. II Fr.* **1992**, *2*, 1941.
(7) Gehlsen, M. D.; Bates, F. S. *Macromolecules* **1993**, *26*, 4122.
(8) Patel, S. S.; Larson, R. G.; Winey, K. I.; Watanabe, H. *Macromolecules* **1995**, *28*, 4313.
(9) Riise, B. L.; Fredrickson, G. H.; Larson, R. G.; Pearson, D. S. *Macromolecules* **1993**, *28*, 7653.
(10) Zhang, Y.; Wiesner, U. *J. Chem. Phys.* **1995**, *103*, 4784.
(11) Johnson, J. M.; Allgaier, J. B.; Wright, S. J.; Young, R. N.; Buzza, N.; McLeish, T. C. B. *J. Chem. Soc., Faraday Trans.* **1995**, *91*, 2403.
(12) Floudas, G.; Paraskeva, S.; Hadjichristidis, N.; Fytas, G.; Chu, B.; Semenov, A. N. *J. Chem. Phys.* **1997**, *107*, 5502.
(13) Chrissopoulou, K.; Tselikas, Y.; Anastasiadis, S. H.; Frytas, G.; Semenov, A. N.; Fleischer, G.; Hadjichristidis, N.; Thomas, E. L. *Macromolecules* **1999**, *32*, 5115.
(14) Milner, S. T.; McLeich, T. C. B. *Macromolecules* **1997**, *30*, 2159.
(15) Milner, S. T.; McLeich, T. C. B. *Macromolecules* **1998**, *31*, 7479.
(16) Iatrou, H.; Hadjichristidis, N. *Macromolecules* **1993**, *26*, 2479.
(17) Quirk, R. P.; Yoo, T.; Lee, B. J. *J. Macromol. Sci.—Pure Appl. Chem.* **1994**, *A31*, 911.
(18) Tsitsilianis, C.; Goulgaris, D. *J. Macromol. Sci.—Pure Appl. Chem.* **1995**, *A32*, 569.
(19) Allgaier, J.; Young, R. N.; Efstratiadis, V.; Hadjichristidis, N. *Macromolecules* **1996**, *29*, 1794.
(20) Ferry, J. D. *Viscoelastic Properties of Polymers*, 3rd ed.; Wiley: New York, 1980.
(21) Olvera de la Cruz, M.; Sanchez, I. C. *Macromolecules* **1986**, *19*, 2501.
(22) Buzza, D. M. A.; Hamley, I. W.; Fzea, A. H.; Moniruzzaman, M.; Allgaier, J. B.; Young, R. N.; Olmsted, P. D.; McLeish, T. C. B.; Lodge, T. P. *Macromolecules* **1999**, *32*, 7483.
(23) Fredrickson, G. H.; Helfand, E. *J. Chem. Phys.* **1987**, *87*, 697.
(24) Mori, K.; Hasegawa, H.; Hashimoto, T. *Polym. J.* **1985**, *17*, 799.
(25) Bras, W.; Derbyshire, G. E.; Ryan, A. J.; Mant, G. R.; Felton, A.; Lewis, R. A.; Hall, C. J.; Greaves, G. N. *Nucl. Instrum. Methods Phys. Rev.* **1993**, *A326*, 587.
(26) Bras, W.; Derbyshire, G. E.; Clarke, S.; Devine, A.; Komanschek, B. U.; Cooke, J.; Ryan, A. J. *J. Appl. Crystallogr.* **1995**, *28*, 26.
(27) Mai, S.-M.; Fairclough, J. P.; Hamley, I. W.; Matsen, M. W.; Denny, R. C.; Liao, B.-X.; Booth, C.; Ryan, A. J. *Macromolecules* **1996**, *29*, 6212.
(28) Matsen, M. W.; Gardiner, J. M. To be published in *J. Chem. Phys.*
(29) Hadziioannou, G.; Skoulios, A. *Macromolecules* **1982**, *15*, 258.
(30) Almdal, K.; Rosedale, J. H.; Bates, F. S.; Wignall, G. D.; Fredrickson, G. H. *Phys. Rev. Lett.* **1990**, *65*, 1112.
(31) Han, C. D.; Kim, J. *J. Polym. Sci. Polym. Phys.* **1987**, *25*, 1741.
(32) Han, C. D.; Kim, J. K. *Polymer* **1993**, *34*, 2533.
(33) Composto, R. J.; Kramer, E. J.; White, D. M. *Polymer* **1990**, *31*, 2320.
(34) Green, P. F.; Adolf, D. B.; Gilliom, L. R. *Macromolecules* **1991**, *24*, 3377.
(35) Lodge, T. P.; McLeish, T. C. B., submitted to *Macromolecules*.
(36) Milhaupt, J. M.; Chapman, B. R.; Lodge, T. P.; Smith, S. D. *J. Polym. Sci. Polym. Phys.* **1998**, *36*, 3079.
(37) Lodge, T. P. Private communication.
(38) Lodge, T. P.; Dalvi, M. C. *Phys. Rev. Lett.* **1995**, *75*, 657.
(39) Hamersky, M. W.; Tirrell, M.; Lodge, T. P. *Langmuir* **1998**, *14*, 6974.
(40) Rubinstein, M.; *Phys. Rev. Lett.* **1986**, *57*, 3023.
(41) Doi, M.; Edwards, S. F. *The Theory of Polymer Dynamics*; Clarendon Press: Oxford, England, 1986.
(42) Fetters, L. J.; Lohse, D. J.; Richter, D.; Witten, T. A.; Zirkel, A. *Macromolecules* **1994**, *27*, 4639.
(43) Kawasaki, K.; Onuki, A. *Phys. Rev. A* **1990**, *42*, 3664.
(44) Fredrickson, G. H.; Bates, F. S. *Annu. Rev. Mater. Sci.* **1996**, *26*, 501.
(45) This of course presupposes that we do not have parallel addition of the domain moduli where the soft phase dominates (e.g., when the lamellae are oriented parallel to the shearing plates). However, we expect this assumption to be valid for our unoriented samples since the microdomains are globally disordered.
(46) The composition and temperature dependences of local friction factors in polymer mixtures is often complicated, and hard to predict on the basis of pure component values.[33-35] On the other hand, for the particular case of styrene—isoprene systems, Milhaupt et al. have shown that the friction factors of the two components are essentially identical in a given matrix, and depend mostly on the distance from the glass transition of the matrix.[36] In the microphase-separated state the situation is further complicated because the friction factors should depend on position, with the largest values corresponding to the regions richest in styrene.